An integrated analysis of contemporary methane emissions and concentration trends over China using in situ, satellite observations, and model simulations

Haiyue Tan[1], Lin Zhang[1], Xiao Lu[2], Yuanhong Zhao[3], Bo Yao[4], Robert J. Parker[5,6], Hartmut Boesch[5,6]

[1]Department of Atmospheric and Oceanic Sciences, School of Physics, Peking University, Beijing, China
[2]School of Atmospheric Sciences, Sun Yat-sen University, Zhuhai, China
[3]College of Oceanic and Atmospheric Sciences, Ocean University of China, Qingdao, China
[4]Meteorological Observation Centre of China Meteorological Administration (MOC/CMA), Beijing, China
[5]National Centre for Earth Observation, University of Leicester, Leicester, UK
[6]Earth Observation Science, School of Physics and Astronomy, University of Leicester, UK

Correspondence to: Lin Zhang (zhanglg@pku.edu.cn)

Abstract.

China, being one of the major emitters of greenhouse gases, has taken strong actions to tackle climate change, e.g., to achieve carbon neutrality by 2060. It also becomes important to better understand the changes in the atmospheric mixing ratios and emissions of CH_4, the second most important human-influenced greenhouse gas, in China. Here we analyze the sources contributing to the atmospheric CH_4 mixing ratios and their trends in China over 2007–2018 using the GEOS-Chem model simulations driven by two commonly used global anthropogenic emission inventories: the Emissions Database for Global Atmospheric Research (EDGAR v4.3.2) and the Community Emissions Data System (CEDS). The model results are interpreted with an ensemble of surface, aircraft, and satellite observations of CH_4 mixing ratios over China and the Pacific region. The EDGAR and CEDS estimates show considerable differences reflecting large uncertainties in estimates of Chinese CH_4 emissions. Chinese CH_4 emission estimates based on EDGAR and natural sources increase from 46.7 Tg per annum (Tg a^{-1}) in 1980 to 69.8 Tg a^{-1} in 2012 with an increase rate of 0.7 Tg a^{-2}, and estimates with CEDS increase from 32.9 Tg a^{-1} in 1980 and 76.7 Tg a^{-1} in 2014 (a much stronger trend of 1.3 Tg a^{-2} over the period). Both surface, aircraft, and satellite measurements indicate CH_4 increase rates of 7.0–8.4 ppbv a^{-1} over China in the recent decade. We find that the model simulation using the CEDS inventory and interannually varying OH levels can best reproduce these observed CH_4 mixing ratios and trends over China. Model results over China are sensitive to the global OH level, with a 10% increase in the global tropospheric volume-weighted mean OH concentration presenting a similar effect to that of a 47 Tg a^{-1} decrease in global CH_4 emissions. We further apply a tagged tracer simulation to quantify the source contributions from different emission sectors and regions. We find that domestic CH_4 emissions account for 14.0% of the mean surface mixing ratio and drive 66.7% of the surface trend (mainly via the energy sector) in China over 2007–2018. We emphasize that intensive CH_4 measurements covering eastern China will help better assess the driving factors of CH_4 mixing ratios and support the emission mitigation in China.

1 Introduction

Atmospheric methane (CH$_4$) is the second most important anthropogenic greenhouse gas contributing more than a quarter of the human-induced radiative imbalance since 1750 (IPCC, 2013). It also plays an important role in atmospheric chemistry as an essential precursor for tropospheric ozone and stratospheric water vapor (Turner et al., 2019). Global mean atmospheric CH$_4$ surface mixing ratios increased from about 1650 ppbv in the mid 1980s to about 1770 ppbv in the late 1990s, then stabilized around this level in the early 2000s, and started increasing again since 2007 (Dlugokencky et al., 2009; Nisbet et al., 2019). The regrowth of the atmospheric CH$_4$ mixing ratio has drawn worldwide attention and led to many different or even contradictory explanations (Zhang et al., 2021; Yin et al., 2021; Zhao et al., 2019; Turner et al., 2019; Maasakkers et al., 2019). Difficulties in the attribution of the trends are mainly associated with large uncertainties in changes in the CH$_4$ emissions from various sources as well as the chemical loss via oxidation by hydroxyl radical (OH) (Turner et al., 2019). A better understanding and quantification of the interannual variability of CH$_4$ emissions and the drivers of the concentration growth in the recent decade is important to support its mitigation.

CH$_4$ has both important anthropogenic and natural sources. It can be emitted from human activities including coal mining, oil and gas exploitation, livestock, rice cultivation, waste deposit, and wastewater treatment. It also has a large natural source from wetlands, with small sources from forest fires, termites, and geological seeps. Global bottom-up estimates of CH$_4$ emissions based on statistics of source activities or process-based models have reported a wide range of total CH$_4$ emissions of 542–852 Tg a^{-1} in the 2000s (Kirschke et al., 2013). Atmospheric top-down analyses constrained by surface, satellite, and aircraft observations of CH$_4$ mixing ratios tend to suggest lower total CH$_4$ emissions of 526–569 Tg a^{-1} in the period (Kirschke et al., 2013) and find even greater uncertainties in the relative contributions from different CH$_4$ emission sectors (Kirschke et al., 2013; Saunois et al., 2016; Saunois et al., 2020). Over 90% of atmospheric CH$_4$ is lost via oxidation by OH in the troposphere, leading to a lifetime of 9.14 ($\pm$10%) years against this sink (IPCC, 2013). Additional minor sinks include soil absorption, loss in the stratosphere, and reactions with chlorine radicals (IPCC, 2013). The contemporary growth of atmospheric CH$_4$ levels reflect an imbalance between its global sources and sinks.

China is one of the most significant methane producers, especially for anthropogenic sources such as coal mining (Saunois et al., 2016). Anthropogenic sources in China contribute about 13% of the global anthropogenic CH$_4$ emissions in the 2000s (Kirschke et al., 2013). The recent bottom-up emission inventory of Peng et al. (2016) found that the total Chinese CH$_4$ emissions increased from 24.4 Tg a^{-1} in 1980 to 45.0 Tg a^{-1} in 2010, with the largest source sector being rice cultivation in 1980 and replaced by coal mining after 2005. However, large uncertainties exist in our understanding of the contemporary changes of CH$_4$ emissions over China (Saunois et al., 2020), e.g., whether the Chinese CH$_4$ emissions from coal mining has

decreased due to the mitigation policy in recent years (Miller et al., 2019; Sheng et al., 2019). Atmospheric inversion analyses are typically applied at global scales due to very limited in situ CH_4 measurements over this region in 2000s. The increases of spatiotemporal observations (from satellite or aircraft) and the development of atmospheric transport models would be helpful in constraining methane sources over China, but different dataset and methods could provide discrepant information (Thompson et al., 2015; Miller et al., 2019). China has pledged to peak the carbon dioxide emissions by 2030 and to reach carbon neutrality by 2060 for tackling climate change. As CH_4 being the second most important anthropogenic greenhouse gas, it also becomes crucial to quantify its emissions and concentration trends in China.

In this study, we aim to better understand the recent trends in CH_4 emissions and mixing ratios in China using the GEOS-Chem (Goddard Earth Observing System-Chemistry) chemical transport model driven by two commonly used global anthropogenic emission inventories: the Emission Database for Global Atmospheric Research (EDGAR, version 4.3.2) (Janssens-Maenhout et al., 2019) and the Community Emissions Data System (CEDS, version 2017-05-18) (Hoesly et al., 2018). We use an ensemble of surface, aircraft, and satellite observations to assess the CH_4 mixing ratios and trends from surface to the troposphere, and conduct a series of model simulations to examine their driving factors as well as the influence of the interannual variability of global volume-weighted OH concentrations. An improved tagged CH_4 tracer simulation (with 100 region- and sector-specific tracers) is applied to identify and quantify the contributions to the spatial patterns of CH_4 mixing ratios and trends over China in the recent decade of 2007–2018.

2 Measurements and the GEOS-Chem model

2.1 Surface and aircraft measurements

We use the surface CH_4 mixing ratio measurements from the Global Monitoring Division (GMD) of the Earth System Research Laboratory (ESRL) at the National Oceanic and Atmospheric Administration (NOAA). The CH_4 mixing ratios are measured by gas chromatography with flame ionization detection (Dlugokencky, 2005). The measurement database (https://www.esrl.noaa.gov/gmd/dv/data/, last access: 3 March 2021) includes 95 sites globally providing monthly averages of mixing ratios (ppbv). The database has been widely used in assessing regional and global CH_4 mixing ratios and budgets (Bergamaschi et al., 2013; Fraser et al., 2013; Cressot et al., 2014; Turner et al., 2016; Miller et al., 2019).

Here we focus on four sites located in China, as summarized in Table 1, including Dongsha Island (DSI, 20.7^o N, 116.7^o E) measuring from March 2010 to December 2018, Lulin (LLN, 23.5^o N, 120.9^o E) from August 2006 to December 2018, Shangdianzi (SDZ, 40.7^o N, 117.1^o E) from September 2009 to September 2015, and Waliguan (WLG, 36.3^o N, 100.9^o E) from May 1991 to December 2018. Three of these sites (LLN, SDZ, and WLG) are mountain-top sites while DSI is located in the

marine boundary layer. The WLG site located in the Qinghai-Tibet Plateau at 3810 m above sea level is the first baseline observatory in China, providing continuous measurements since the year 1991.

We analyze measurements of CH_4 mixing ratios from two aircraft campaigns: the High-performance Instrumented Airborne Platform for Environmental Research (HIAPER) Pole-to-Pole observation (HIPPO) and the Atmospheric Tomography Mission (ATom). HIPPO consists of five campaigns from January 2009 to September 2011 (Wofsy et al., 2011). ATom consists of four campaigns from July 2016 to May 2018 (Wofsy et al., 2018). Figure 1 shows the flight tracks from two campaigns. Both HIPPO and ATom datasets provide the merged 10-second data products for all flights (Wofsy et al., 2017; Wofsy et al., 2018), which cover the four seasons temporally and the regions over the Pacific Ocean and North America spatially. Both campaigns provide global-scale measurements of atmospheric composition in all seasons, and conduct continuous profiling between ~0.15 km and 8.5 km altitude with many profiles extending to nearly 14 km. Here we sample the model results at the hourly resolution along flight tracks as shown in Fig. 1 and average them in 2° latitude bins for the comparison.

2.2 GOSAT satellite observations

The TANSO-FTS instrument onboard the Greenhouse Gases Observing Satellite (GOSAT) launched in early 2009 measures the backscattered solar radiation from a sun-synchronous orbit at around 13:00 local time (Butz et al., 2011; Kuze et al., 2016). The observations have a pixel resolution of around 10 km diameter and are separated by about 250 km along the observing track with a global coverage every 3 days (Parker et al., 2015). GOSAT retrieves column-averaged dry-air CO_2 and CH_4 mixing ratios from the shortwave infrared (SWIR) spectrum with near-unit sensitivity down to the surface (Butz et al., 2011). We use the University of Leicester version 7.2 GOSAT XCH_4 proxy retrieval over China from January 2010 to December 2017. The glint data over the oceans are not used in this study due to the sparse data coverage. The CH_4 product has been validated by Parker et al. (2015) against the Total Carbon Column Observing Network (TCCON) and MACC-II model XCH4 data and suggested a precision of 0.7%.

To compare with the GEOS-Chem model results as described below, the GOSAT CH_4 observations and satellite averaging kernels are averaged over the 2°×2.5° or 4°×5° model grid. We use the satellite observations which pass the criteria that the grid has more than 12 months of valid observations which have passed their quality control. The simulated vertical profiles (VMR^{mod}) are applied with the satellite averaging kernels (AK) and a priori estimates (VMR^{apr}) using Equ. (1) following Parker et al. (2020).

$$XCH_4^{mod} = \sum_{i=0}^{N_{lev}}\{[VMR_i^{apr} + (VMR_i^{mod} - VMR_i^{apr})AK_i]h_i\} \quad (1)$$

where AK_i is the retrieval averaging kernel and h_i is the pressure weight for the vertical level i. This provides column mean CH_4 mixing ratios (XCH_4^{mod}) with the vertical sensitivity of satellite retrievals accounted for.

2.3 The GEOS-Chem model description and simulation design

We use the GEOS-Chem global chemical transport model v11-02 release candidate (http://geos-chem.org, last access: 3 March 2021) driven by MERRA-2 meteorological fields from the NASA Global Modeling and Assimilation Office (GMAO). The MERRA-2 dataset has a native horizontal resolution of 0.5° latitude×0.625° longitude, and is degraded to 4°×5° or 2°×2.5° resolutions for input to GEOS-Chem. We use the CH_4 simulation that calculates the CH_4 sinks using prescribed global distributions of OH concentrations or loss frequencies. The model has been applied in a number of studies to understand the global and regional CH_4 emissions and mixing ratios (Wecht et al., 2014; Turner et al., 2015; Maasakkers et al., 2019; Lu et al., 2021; Maasakkers et al., 2021; Zhang et al., 2021). All the simulations are initiated in the year 1980 and we focus on the model results in the period of 2007–2018. We find that changes in the initial CH_4 conditions in January 1980 would not affect simulation results after January 2000, indicating that a spin-up time of over 20 years is sufficient for our analyses.

We use and compare two global anthropogenic CH_4 inventories: the Emissions Database for Global Atmospheric Research (EDGAR v4.3.2) covering 1970–2012 (Janssens-Maenhout et al., 2019) and the Community Emissions Data System (CEDS, version 2017-05-18) (Hoesly et al., 2018) covering 1970–2014. A detailed comparison of the two emission estimates will be presented in Section 3. The EDGAR CH_4 emissions do not account for seasonal variations. Here we have applied seasonal scalars to CH_4 emissions from manure management based on a temperature dependence described by Maasakkers et al. (2016) and to those from rice cultivation following Zhang et al. (2016) in the EDGAR inventory. The CEDS inventory as used in this study provides gridded emission estimates with monthly variations.

For natural sources, monthly wetland emissions are from the WetCHARTs version 1.0 extended ensemble mean for 2001–2015 (Bloom et al., 2017) and are scaled by 1.1 to match the estimates in Kirschke et al. (2013) and Saunois et al. (2020). Open fire emissions are from the Quick Fire Emissions Database version 2.4 with daily variability over 2009–2015 (Darmenov and Da Silva, 2013). Termite and seepage emissions are, respectively, from Fung et al. (1991) and Maasakkers et al. (2019).

The oxidation of CH_4 by tropospheric OH is calculated in the model using 3-D monthly averaged OH concentrations archived from a standard GEOS-Chem tropospheric chemistry simulation in Wecht et al. (2014). Global uniform scalers are then applied to account for the interannual variability of OH concentrations during 1980–2010 as simulated by the CESM model in Zhao et al. (2019). As shown in Fig. S1, the resulting global volume-weighted mean OH increases by 0.20% a^{-1} in 1980–2000 and 0.37% a^{-1} in 2000–2010, finally reaching to 10.9×10^5 molecules cm^{-3}. Other minor sinks include tropospheric oxidation by chlorine atoms using monthly chlorine concentration fields of Sherwen et al. (2016), stratospheric loss computed with monthly loss frequencies of Murray et al. (2012), and soil uptake of Fung et al. (1991) with a temperature dependent seasonality (Ridgwell et al., 1999).

We have conducted a series of model simulations over 1980–2018 as summarized in Table 1 to investigate the impacts of OH concentrations and model resolution. For all the datasets of emissions (using EDGAR and CEDS) and sinks as described above, the closest available year will be used for simulation years beyond their available time ranges as recent studies suggested weak trends in Chinese CH_4 emissions after 2010 (Sheng et al., 2021; Liu et al., 2021). Since CH_4 has a long lifetime of about 9 years, model results in the later years (e.g., after 2012 for EDGAR and after 2014 for CEDS) are strongly affected by the emissions in earlier years. Evaluations of these model results with the NOAA surface measurements at the four Chinese sites indicate that the simulation with CEDS and interannually varying OH at $2° \times 2.5°$ resolution (GCC in Table 1) relatively better captures the measured mixing ratios and trends since 2007, as will be discussed in Section 3.2.

We further apply a tagged CH_4 tracer simulation to quantify the sources contributing to CH_4 mixing ratios and trends in China over 2007–2018. The tagged CH_4 tracer approach has been recently applied in GEOS-Chem to quantify source contributions in U.S. Midwest (Yu et al., 2021) and GFDL-AM4.1 with focuses on the global CH_4 budget (He et al., 2020). We implement 100 tracers that tag CH_4 emissions from different source types (agriculture, energy, industry, transportation, wastewater, residents, shipping, biomass burning, wetlands, seeps and termites) and different regions (China, India, Europe, South America, North America, Africa, Oceania, etc.). The regions used for the tagged simulation are shown in Fig.2, mainly based on Bey et al. (2001) with additional tagged regions for China and India in Asia. Global soil uptake is also tagged as a sink of CH_4. We run the tagged CH_4 simulation using the model settings of GCC (i.e., CEDS and interannually varying OH) for the period of 1980–2018. The results allow us to quantify the detailed source contributions to CH_4 mixing ratios and trends over China.

3 Results

3.1 CH_4 emissions and sinks over the globe and China

Figure 3 and Supplementary Table S1 compare the anthropogenic emissions of EDGAR and CEDS, natural emissions, and sinks in our model simulations (GCE and GCC in Table 1) with the estimates in the literature summarized by Saunois et al. (2020). The emissions in the two decades of 2000–2009 and 2008–2017 from both bottom-up and top-down studies are reported in Saunois et al. (2016; 2020), and are thus compared with corresponding estimates in this study. The anthropogenic emission source categories are different in the EDGAR and CEDS inventories, and we organize all sources into five main categories (agriculture and waste, biomass burning, fossil fuels, wetlands, and other sources) following Saunois et al. (2020), as also summarized in Table S2.

As shown in Fig. 3, the global total (anthropogenic and natural) emissions over 2000–2009 are 520 Tg a^{-1} for GCE and 533 Tg a^{-1} for GCC. These total emissions are in the low end of the top-down estimates of 547 Tg a^{-1} with a range of 524–560 Tg

a^{-1}, and are smaller than the bottom-up estimates of 703 (566–842) Tg a^{-1}. The bottom-up estimates summarized by Saunois et al. (2020) included EDGAR and CEDS, and we can see that the differences with our emissions are largely driven by the underestimates of some natural emissions (e.g., geological, termites, and freshwaters emissions), which are substantially reduced in the top-down estimates. In the 2008–2017 period, global total CH_4 emissions in GCE and GCC have increased to

95   556 Tg a^{-1} in GCE and to 574 Tg a^{-1} in GCC, and are within the top-down emission range of 576 (550-594) Tg a^{-1}. The contributions of anthropogenic sources on total CH_4 emissions are about 63% (2000–2009) and 65% (2008–2017) in GCE, and 65% (2000–2009) and 67% (2008–2017) in GCC, which are slightly larger than 60% and 62% in the top-down estimates of Saunois et al. (2020). The global CH_4 chemical losses simulated in GCE and GCC are also consistent with the top-down estimates for both periods, while the sink of soil uptake might be underestimated in the model.

00

Table 2 and Fig. 4 compare the annual CH_4 emissions and sinks in China simulated in GCE and GCC with the results reviewed by Saunois et al. (2020) and Kirschke et al. (2013) and a bottom-up anthropogenic emission inventory of Peng et al. (2016) for the period of 2000–2009. Total Chinese CH_4 emissions are 57.2 Tg a^{-1} (2000–2009) and 67.6 Tg a^{-1} (2008–2017) in GCE, and 55.5 Tg a^{-1} (2000–2009) and 73.7 Tg a^{-1} (2008–2017) in GCC. Considerable differences between GCE and GCC can be

05   seen for the emission estimates of different sectors. The CH_4 emissions from fossil fuels over 2000–2009 are 23.4 Tg a^{-1} in GCC, which are at the high end of the bottom-up estimates (12.6–23.9 Tg a^{-1}) summarized in Saunois et al. (2020). The CH_4 emissions from fossil fuels in GCE are smaller (15.8 Tg a^{-1} over 2000–2009), and are slightly higher than the estimate of 12.8 in Peng et al. (2016). By contrast, CH_4 emissions from agricultural and waste in GCE (33.3 Tg a^{-1} over 2000–2009) are much higher than those in GCC (25.3 Tg a^{-1} over 2000–2009), and they are, respectively, at the high and low ends of the bottom-up

10   (24.0–33.0 Tg a^{-1}) estimates in Saunois et al. (2020). The natural sources (e.g., wetlands, biomass burning) and the soil uptake in our study are relatively low compared with the estimates in Saunois et al. (2020). For the period of 2008–2017, the CH_4 emissions from fossil fuels increase to 22.8 Tg a^{-1} in GCE and 38.4 Tg a^{-1} in GCC, which are also at the averaged level and the high end of the bottom-up estimate (16.6–39.6 Tg a^{-1}) in Saunois et al. (2020).

15   Figure 5 further shows annual total Chinese CH_4 emissions from different sectors and their percentage contributions during 1980–2018 in both GCE and GCC simulations. Chinese total CH_4 emissions in GCE are 46.7 Tg a^{-1} in the year 1980 and increase to 69.8 Tg a^{-1} (49.5% increase) in 2012 (the last available year for EDGAR v4.3.2), presenting an increase trend of 0.7 Tg a^{-2} over 1980–2018. GCC simulations have a stronger trend of 1.3 Tg a^{-2} over the period than GCE, with total emissions of 32.9 Tg a^{-1} in 1980 and 76.7 Tg a^{-1} in 2014 (the last available year of CEDS). Both GCE and GCC show faster increases

20   after 2003 than the years before, which are largely driven by the emissions from the fossil fuels or energy sector. The largest differences between GCE and GCC, as also discussed in Fig. 4, come from the sectors of fossil fuels and agriculture. Agriculture sources in GCE account for 54.7% of the total CH_4 emissions in 1980 and gradually decrease to 37.0% in 2018, which mainly result from decreases in emissions from rice cultivation with some offset due to increases in the livestock

emission. The contributions of agricultural sources in GCC are much smaller with values of 36.3% in 1980 and 21.5% in 2018.

25 The energy or fossil fuels sector becomes the largest contributor of Chinese CH_4 emissions in recent years in GCC, accounting for 52.2% of the total emissions in 2018, and largely drives the larger positive trend in GCC than GCE.

The comparisons above indicate large uncertainties in the Chinese CH_4 emission estimates, as to some extent covered by the EDGAR and CEDS anthropogenic emission inventories. The magnitude and temporal variations of methane budgets over the

30 past decades are known to have large uncertainties (Kirschke et al., 2013; Turner et al., 2019; Saunois et al., 2020). Relative uncertainties are about 20–35% for anthropogenic emissions such as fuel exploitation, agriculture and waste, about 50% for biomass burning and wetlands, and reach 100% or greater for other natural sources (Saunois et al., 2020). Uncertainties in the methane sinks are about 10–20% by proxy methods such as using methyl chloroform, and are 20–40% by atmospheric chemistry models (Saunois et al., 2016). More detailed regional methane datasets can help improve assessing the global budget

35 (Xu and Tian, 2012; Valentini et al., 2014; Saunois et al., 2016). We will further discuss the uncertainties in CH_4 emissions in the last section.

3.2 Observed and simulated methane mixing ratios and trends in China

Based on the emissions described above, we have conducted a series of model simulations as summarized in Table 1 and evaluated the model results with surface CH_4 measurements at the four Chinese sites. We find that when using the interannually

40 fixed OH (global tropospheric volume-weighted mean of 10.6×10^5 molecules cm^{-3} as shown in Fig. S1), both model simulations with the EDGAR and CEDS emissions overestimate the observed CH_4 trends since 2007 by 0.8–6.2 ppbv a^{-1} with EDGAR (Run1) and by 4.0–10.9 ppbv a^{-1} with CEDS (Run2). The model simulated CH_4 mixing ratios and trends over China are rather sensitive to the global OH levels. In the sensitivity simulations with global OH decreasing 10% (Run5) or increasing 10% (Run6) relative to the fixed levels (global mean of 10.9×10^5 molecules cm^{-3}) over 2010–2018, CH_4 mixing ratios would,

45 respectively, increase by 2.0%–3.4% or decrease 1.9%–3.2% at the four Chinese sites (Fig. S2). Increasing OH levels by 10% would lead negative trends in CH_4 mixing ratios at all four sites over 2010–2018 (Fig. S2). Such effects are also found in the simulation with global CH_4 emissions decreasing 50 Tg a^{-1} over the same period (Run 7 in Table 1 and Fig. S2).

The uses of interannually varying OH (Fig. S1) in model simulations (Run3 and Run4 in Table 1) overall correct the high

50 biases in simulated CH_4 trends in simulations with fixed OH (Run1 and Run2) at the Chinese sites. We find that changing model horizontal resolution from 4°×5° to 2°×2.5° does not significantly affect the simulated surface CH_4 trends. Hereafter, we will focus our analyses on the model simulations at 2°×2.5° resolution and with interannually varying OH (i.e., GCE and GCC in Table 1).

Figure 6 shows the measured and simulated time series of monthly CH$_4$ mixing ratios at the four Chinese sites. Both GCE and GCC model results are shown, and distinct differences in CH$_4$ mixing ratios can be seen between the two simulations. Among the four Chinese sites, the largest CH$_4$ mixing ratio is observed at the SDZ site, a rural site near Beijing surrounded by high anthropogenic emissions, compared with the other three Chinese background sites (DSI, LLN, and WLG). GCC with high anthropogenic emission estimates simulate on average 1.0%–4.7% higher CH$_4$ mixing ratios than GCE results, and are 0.3%–6.5% higher than measurements at the four Chinese sites. Measured CH$_4$ mixing ratios at the four sites are increasing at the rates of 7.0–7.9 ppbv a^{-1} in recent years since 2007. The GCC model results reproduce the trends in CH$_4$ mixing ratios at the DSI, LLN, and WLG sites, while overestimate the 2009–2015 trend measured at SDZ by a factor of two. The GCE model results in general underestimate the measured trends except for that at the SDZ site. These results can be explained by the higher CH$_4$ emission estimates and increases in CEDS than EDGAR since 2007, and may also reflect the regional CH$_4$ emissions around SDZ (i.e., North China) are too high in CEDS. Further evaluations of the two model simulations with CH$_4$ column mixing ratio measurements (since 2011) at six TCCON sites in Asia (Wunch et al., 2011) show similar results, with small biases of 0.2%–1.0% in CH$_4$ mixing ratios for GCC and negative biases of 2.6%–3.7% for GCE (Fig. S3). This again reflects the higher Chinese CH$_4$ emission estimates in years around 2012 in CEDS than EDGAR, which then affect the model simulations afterwards by using their emissions of the latest available years.

Comparisons with satellite and aircraft observations further provide spatially and vertically resolved evaluations of the model simulations. Figures 7 and 8 show, respectively, the GOSAT observed and model simulated spatial distributions of seasonal mean CH$_4$ mixing ratios and trends over 2010–2017. The latitude-dependent biases between simulations and observations have found noticeable at the 4°×5° resolution, but is significantly smaller at 2°×2.5° (Stanevich et al., 2020). The GOSAT observed CH$_4$ column mixing ratios over China peak in autumn (1825.6 ppbv on average) and reach a minimum in spring (1797.4 ppbv). There is a stronger seasonality in the CH$_4$ mixing ratio in the South China (1856.9 ppbv in autumn vs. 1826.8 ppbv in spring) likely attributed to the seasonal variation in agriculture emissions. The GOSAT observed 2010–2017 trends show small spatial and seasonal variations over China with values of 7.67–8.43 ppbv a^{-1}. Both GCE and GCC model simulated CH$_4$ mixing ratios present similar spatial patterns with high correlation coefficients (r > 0.90), while GCE simulated mixing ratios are on average biased low by 23.5–32.4 ppbv (~1.6%), and GCC results are overestimated by 25.6–36.8 ppbv (~1.7%). This discrepancy between the two simulations is mainly due to the CH$_4$ emissions from fossil fuels, which are 23.5 Tg a^{-1} for the GCE and 39.9 Tg a^{-1} for the GCC in China over 2010–2017. As for the CH$_4$ trends during 2010–2017 over China, both GCC and GCE show similar spatial patterns as those observed by GOSAT with moderate correlations of 0.2–0.5, while GCC model results have smaller biases of −1.7–0.4 ppbv a^{-1}, compared to GCE results that in general underestimate the trends by 2.6–4.7 ppbv a^{-1}.

Figure 9 shows the latitudinal distribution of annual mean CH$_4$ mixing ratios as observed by HIPPO and ATom aircraft campaigns at three altitude layers (1–2 km, 4–5 km, and 7–8 km). Model results sampled along the flight tracks at their

observing time are also shown. Both aircraft measurements and model results are then averaged in 2° latitude bins. As shown in Fig. 9, large latitudinal gradients in the tropospheric CH_4 mixing ratios between the northern and southern hemispheres, in

90 particular in the lowest 2 km of the tropics, are observed by the aircraft measurements, and are captured by the model results with the two emission inventories. Similar to the comparison with GOSAT observations, GCE model simulated CH_4 mixing ratios tend to be lower than those in GCC due to the lower estimate of global emissions in GCE (556 Tg a^{-1}) than GCC (574 Tg a^{-1}) since 2008 (Table S1). GCE model results underestimate the aircraft measurements with mean negative biases of 27.5–31.1 ppbv at the three altitude layers for HIPPO, and even larger negative biases of 61.5–73.7 ppbv for ATom. By contrast,

95 GCC model results are in general too high with biases of 18.4–22.8 ppbv for HIPPO, and −1.7–9.4 ppbv for ATom. The biases in GCC are overall smaller than those in GCE.

The changes in the model bias for the comparisons with HIPPO and ATom measurements reflect their simulated trends in the CH_4 mixing ratios. Since both HIPPO (2009–2011) and ATom (2016–2018) provide measurements over the Pacific (black

00 box in Fig. 1), we calculate the differences between HIPPO and ATom measurements as the observed CH_4 concentration trends over this region, and these trends also largely reflect the influences from upwind Asian CH_4 sources and levels. Figure 10 shows aircraft observed and corresponding model simulated trends separated for four seasons. The HIPPO (2009–2011)–ATom (2016–2018) CH_4 trends as estimated by the aircraft measurements range 5.8–10.7 ppbv a^{-1} for the different seasons and altitudes, with typically higher increasing rates in boreal summer and autumn than those in boreal spring and winter. Both

05 GCE and GCC model results tend to underestimate the trends, but the biases in GCC are much smaller than GCE. A distinct feature can be seen from aircraft observations is the high CH_4 increasing rates over the tropics in boreal summer and autumn (reaching 15 ppbv a^{-1}), while both model results do not capture it and show weak latitudinal gradients in the CH_4 trends. These tropical CH_4 increases are likely driven by the increasing tropical microbial emissions either from wetlands or livestock shown in some recent papers (Nisbet et al., 2016; Saunois et al., 2017; Worden et al., 2017; Maasakkers et al., 2019; Yin et al., 2021;

10 Zhang et al., 2021), which have not been found in the model simulations.

Summarizing the comparisons of model results with all available measurements over China and the Pacific, we find that the surface, aircraft, and satellite CH_4 measurements have indicated rather consistent increase rates of CH_4 mixing ratios over China with values ranging 7.0–8.4 ppbv a^{-1} in recent years. As CH_4 has a lifetime of about 9 years, such increases reflect

15 changes in not only domestic emissions but also global emissions. The GCE and GCC model simulations with the interannually varying OH levels both capture the main features of the observed CH_4 mixing ratios and trends over China, and the GCC results show much smaller model biases than GCE. We will thus use the GCC model simulation to quantify the domestic and global sources contributing to the CH_4 mixing ratios and trends over China.

3.3 Source attribution of CH_4 mixing ratios and trends in 2007–2018

20   Here we apply the GCC model configuration (i.e., the CEDS inventory and interannually varying OH) in the tagged CH_4 simulation. The GCC model results can generally reproduce the spatial distribution of GOSAT observed CH_4 levels and trends as shown in Fig. S4, with mean biases of 27.4 ppbv (observed 1805 ppbv vs. simulated 1833 ppbv) in the global CH_4 mixing ratio and -0.8 ppbv a^{-1} (observed 7.08 ppbv a^{-1} vs. simulated 6.26 ppbv a^{-1}) in the trend. As described in the Section 2.3, our tagged CH_4 simulation includes 100 region- and sector-specific CH_4 tracers. The tagged CH_4 simulation is conducted over

25   1980–2018, and we analyze the results for 2007–2018.   Figure 11 shows contributions of CH_4 emissions from different source regions and different sectors on the mean surface mixing ratios and trends in China during this time period, and the values are also summarized in Table 3 for mixing ratios and Table 4 for trends. As for mixing ratios, we find that the largest contributor of the Chinese CH_4 mixing ratio averaged over 2007–2018 is the wetland emission in South America, accounting for 10.5% due to the large emission magnitude. Together with other sources, emissions in South America contribute 20.2% of the surface

30   CH_4 levels over China, followed by the sources from Africa (17.0%) and Europe (15.0%). The Chinese domestic emissions account for 14.0% of the CH_4 mixing ratio. The emission contributions to the mixing ratio are generally proportional to their emission magnitudes because of the CH_4 lifetime of about 9 years, and seasonal variations in the percentage contributions are small as can be seen in Fig. 11 (the top left panel).

35   Figure 11 and Table 4 also show the source contributions to the 2007–2018 trends in the surface CH_4 mixing ratio over China. Based on the emission inventory in GCC, the simulated mean trend in the surface CH_4 mixing ratio is 9.75 ppbv a^{-1} over the land of China. The domestic energy sector is identified as the largest driver of the trend in China contributing an increase rate of 5.54 ppbv a^{-1}. Accounting for the trends driven by emissions from agriculture and wastewater sectors, domestic contributions can reach 6.50 ppbv a^{-1} (67% of 9.75 ppbv a^{-1}). The remaining trends of 3.25 ppbv a^{-1} are then contributed by

40   emission changes outside China. We find that the anthropogenic sources (mainly from energy, agriculture and wastewater sectors) in Africa and other Asian regions (India and Rest Asia) contribute, respectively, trends of 3.25 and 2.45 ppbv a^{-1} over China, highlighting the strong CH_4 emission increases in these regions such as large emission increases from livestock sources over South Asia and tropical Africa in 2010–2018 (Zhang et al., 2021). On the contrary, Europe is the only region where CH_4 emissions from nearly all sectors have been decreasing (Jackson et al., 2020), which lead to a negative trend of -1.81 ppbv a^{-1}

45   over China. We find strong spatial variation in the contribution values over different regions of China with standard deviations up to 11% for the contributions to CH_4 mixing ratios and up to 0.4 ppbv a^{-1} to the trends (Fig. 11). Not only near the surface, we find similar results for the CH_4 mixing ratios throughout the troposphere over China with slightly smaller growth rates in the upper troposphere (Fig. S5).

50   Our results indicate that trends in China are dominated by energy emissions from coal, oil and gas, with significant contributions from wastewater and agriculture sectors. This is consistent with the top-down emission inversion results by

Miller et al., (2019) that found the Chinese coal emission is increasing in 2010–2015, while the bottom-up emission estimates of Sheng et al. (2019) suggested decreases in the coal emission in 2012–2016. The lack of sub-country emission factors may result in large uncertainties in the bottom-up emission estimates. A recent global emission inversion study using the EDGAR v4.3.2 inventory as the prior estimate also found large overestimates in the Chinese emissions from coal (Maasakkers et al., 2019). Using the overestimated emissions from the domestic coal sector in the model would offset the influence of missing increases in microbial emissions in the tropics as discussed in Section 3.2.

The analyses above demonstrate strong foreign source contributions to the CH_4 mixing ratios as well as CH_4 trends over China. We further find large spatial heterogeneity in the domestic vs. foreign contributions. Figure 12 shows the spatial distributions of domestic emission contributions to Chinese CH_4 surface mixing ratios and trends over 2007–2018 calculated as the percentages of sums of all Chinese tagged tracers to the total levels. We can see that the domestic contribution to the CH_4 surface mixing ratio ranges from 12.4% in the western China to 15.1% in central China, and to the trends ranges from 62.6% over the Tibet Plateau to 70.1% in the central China. The largest domestic contributions for both surface mixing ratios and trends are found in the central eastern China, so that measurements over this region would most reflect the CH_4 emission changes in China.

4 Conclusions and discussion

In summary, we have investigated the sources contributing to the CH_4 mixing ratios and trends over China in the recent decade (2007–2018) using the GEOS-Chem global model. The CH_4 model simulations are conducted considering two different commonly used anthropogenic emission inventories (EDGAR v4.3.2 and CEDS), and are evaluated with available surface, aircraft, and satellite measurements of CH_4 mixing ratios over China and the Pacific region. The surface, aircraft, and satellite measurements have shown CH_4 concentration increase rates of 7.0–8.4 ppbv a^{-1} over China in recent years. We find that model results are sensitive to the selection of anthropogenic emission inventories and OH levels. By using the CEDS anthropogenic emission inventory and interannually varying OH levels (Fig. S2) the model can generally reproduce the measured CH_4 mixing ratios and trends over China. This corresponds to mean Chinese anthropogenic CH_4 emissions of 69.4 Tg a^{-1} (with an increase rate of 1.2 Tg a^{-2}), and global tropospheric volume-weighted mean OH concentrations of 10.8×10^5 molecule cm^{-3} (with an increase rate of 0.25% a^{-1}) over 2007–2018.

We apply a tagged CH_4 tracer simulation that implements region- and sector-specific tracers to diagnose and to understand their emission contributions. Using the model simulation with CEDS and interannually varying OH, we find strong influences from foreign sources on both CH_4 mixing ratios and recent increases over China due to the long lifetime of CH_4. For the mean surface CH_4 mixing ratio over China (1873.0 ppbv over 2007–2018), domestic CH_4 emissions account for 14.0%, and contributions from the sources outside China reaching 86.0%, including 20.2% from South America, 17.0% from Africa, 15.0%

from Europe, 13.0% from North America, and 12.8% from the Rest Asia. For the mean CH_4 concentration trend over China (9.75 ppbv a^{-1} over 2007–2018), the largest driver is estimated to be the domestic energy source contributing 5.54 ppbv a^{-1}, and other important domestic source contributions include emissions from wastewater (0.68 ppbv a^{-1}) and agriculture (0.30 ppbv a^{-1}); natural sources such as wetland emissions have insignificant trend contributions. Emission changes in foreign sources are also significant. The increase rate of 3.14 ppbv a^{-1} in the Chinese surface CH_4 mixing ratio can be attributed to sources in other Asia countries (India and Rest Asia), 1.64 ppbv a^{-1} to Africa, and 0.95 ppbv a^{-1} to South America (Table 4).

It shall be noted that our source attribution results can be biased by the use of CEDS and the uncertainty in the interannual variations of OH levels. The Chinese anthropogenic CH_4 emissions in the CEDS inventory are higher and increase more rapidly than EDGAR v4.3.2 in the recent decade. The two emission inventories significantly differ in the sectors of fossil fuels and agriculture. CEDS estimates higher CH_4 emissions from fossil fuels while lower emissions from agriculture compared with EDGAR v4.3.2. A number of top-down emission inversion studies using surface and satellite observations have found that the EDGAR v4.3.2 (Maasakkers et al., 2019; Miller et al., 2019) and previous EDGAR versions (Alexe et al., 2015; Thompson et al., 2015; Turner et al., 2015; Pandey et al., 2016) overestimated the CH_4 emissions from coal production in China, likely due to the CH_4 emission factors for coal mining are too high in the region (Peng et al., 2016). A recent bottom-up estimate suggested that Chinese coal mining CH_4 emissions have been decreasing since 2012 driven by the China's coal mine regulation (Sheng et al., 2019), but the interannual trend in Chinese coal emissions still has large uncertainties among studies (Miller et al., 2019; Sheng et al., 2019; Lu et al., 2021).

We also find that the interannual variability of OH concentrations can strongly affect the simulated CH_4 concentration trends. Using interannually fixed OH concentrations, the model would overestimate the observed CH_4 growth since 2007 in China with both the EDGAR and CEDS anthropogenic emissions. The influence of a 10% increase in the global volume-weighted mean OH concentration (from 10.9×10^5 molecule cm^{-3} to 12.0×10^5 molecule cm^{-3}) on the simulated Chinese CH_4 mixing ratios is equivalent to that of a 47 Tg a^{-1} decrease in global CH_4 emissions. The use of interannual variability of OH provided by Zhao et al. (2019) improve the model simulated Chinese CH_4 mixing ratios and trends. However, large discrepancies exist in the different model OH simulations that would lead to a large wide range (>±30 ppbv) of simulated CH_4 mixing ratios (Zhao et al., 2019). Despite these uncertainties, our study emphasizes the importance of emission changes in both domestic and foreign, anthropogenic and natural sources on the Chinese CH_4 concentration trends. Future work with more intensive CH_4 measurements covering the eastern China will help better assess the driving factors of Chinese CH_4 mixing ratios and recent growth.

Data availability

NOAA surface observations are available online (https://www.esrl.noaa.gov/gmd/dv/data/, last access: 5 May 2021). The GOSAT Proxy XCH_4 data can be accessed through the Copernicus C3S Climate Data Store at https://cds.climate.copernicus.eu. TCCON data were obtained from the TCCON Data Archive hosted by CaltechDATA through https://tccondata.org/ (last access: 22 November, 2021). The HIPPO data used in this study can be requested through https://www.eol.ucar.edu/field_projects/hippo (last access: 5 May, 2021). The ATom data is available at https://daac.ornl.gov/cgi-bin/dsviewer.pl?ds_id=1581 (last access: 5 May, 2021). Modelling dataset can be accessed by contacting the corresponding author.

Author contributions

HYT and LZ designed the study. HYT conducted the modeling and data analyses with contributions from LZ, XL, YHZ and BY. RJP and HB provided the GOSAT CH_4 data and contributed to the interpretation and discussion of its use in the study. HYT and LZ wrote the paper with input from all authors.

Competing interests

The authors declare that they have no conflict of interest.

Acknowledgments

This work was supported by the National Natural Science Foundation of China (NSFC, 41475112, 41922037) and the National Key Research and Development Program of China (2017YFC0210102). RJP and HB are funded via the UK National Centre for Earth Observation (NE/N018079/1 and NE/R016518/1). We thank the Japanese Aerospace Exploration Agency, National Institute for Environmental Studies, and the Ministry of Environment for the GOSAT data and their continuous support as part of the Joint Research Agreement. This research used the ALICE High Performance Computing Facility at the University of Leicester for the GOSAT retrievals. We thank Kathryn McKain and Steven C. Wofsy for offering the CH_4 dataset from ATom campaigns.

References

Alexe, M., Bergamaschi, P., Segers, A., Detmers, R., Butz, A., Hasekamp, O., Guerlet, S., Parker, R., Boesch, H., Frankenberg, C., Scheepmaker, R. A., Dlugokencky, E., Sweeney, C., Wofsy, S. C., and Kort, E. A.: Inverse modelling of CH_4 emissions

for 2010–2011 using different satellite retrieval products from GOSAT and SCIAMACHY, Atmos. Chem. Phys., 15, 113-133, 10.5194/acp-15-113-2015, 2015.

Bergamaschi, P., Houweling, S., Segers, A., Krol, M., Frankenberg, C., Scheepmaker, R. A., Dlugokencky, E., Wofsy, S. C., Kort, E. A., Sweeney, C., Schuck, T., Brenninkmeijer, C., Chen, H., Beck, V., and Gerbig, C.: Atmospheric CH_4 in the first decade of the 21st century: Inverse modeling analysis using SCIAMACHY satellite retrievals and NOAA surface measurements, J. Geophys. Res.-Atmos., 118, 7350-7369, 10.1002/jgrd.50480, 2013.

Bey, I., Jacob, D. J., Logan, J. A., and Yantosca, R. M.: Asian chemical outflow to the Pacific in spring: Origins, pathways, and budgets, J. Geophys. Res.-Atmos., 106, 23097-23113, 10.1029/2001jd000806, 2001.

Bloom, A. A., Bowman, K. W., Lee, M., Turner, A. J., Schroeder, R., Worden, J. R., Weidner, R., McDonald, K. C., and Jacob, D. J.: A global wetland methane emissions and uncertainty dataset for atmospheric chemical transport models (WetCHARTs version 1.0), Geosci. Model Dev., 10, 2141-2156, 10.5194/gmd-10-2141-2017, 2017.

Butz, A., Guerlet, S., Hasekamp, O., Schepers, D., Galli, A., Aben, I., Frankenberg, C., Hartmann, J. M., Tran, H., Kuze, A., Keppel-Aleks, G., Toon, G., Wunch, D., Wennberg, P., Deutscher, N., Griffith, D., Macatangay, R., Messerschmidt, J., Notholt, J., and Warneke, T.: Toward accurate CO_2 and CH_4 observations from GOSAT, Geophys. Res. Lett., 38, n/a-n/a, 10.1029/2011gl047888, 2011.

Cressot, C., Chevallier, F., Bousquet, P., Crevoisier, C., Dlugokencky, E. J., Fortems-Cheiney, A., Frankenberg, C., Parker, R., Pison, I., Scheepmaker, R. A., Montzka, S. A., Krummel, P. B., Steele, L. P., and Langenfelds, R. L.: On the consistency between global and regional methane emissions inferred from SCIAMACHY, TANSO-FTS, IASI and surface measurements, Atmos. Chem. Phys., 14, 577-592, 10.5194/acp-14-577-2014, 2014.

Darmenov, A. and da Silva, A.: The quick fire emissions dataset (QFED)–documentation of versions 2.1, 2.2 and 2.4, NASA Technical Report Series on Global Modeling and Data Assimilation, NASA TM-2013-10460632, 183pp., 2013.

Dlugokencky, E. J.: Conversion of NOAA atmospheric dry air CH_4 mole fractions to a gravimetrically prepared standard scale, J. Geophys. Res., 110, 10.1029/2005jd006035, 2005.

Dlugokencky, E. J., Bruhwiler, L., White, J. W. C., Emmons, L. K., Novelli, P. C., Montzka, S. A., Masarie, K. A., Lang, P. M., Crotwell, A. M., and Miller, J. B.: Observational constraints on recent increases in the atmospheric CH_4 burden, Geophys. Res. Lett., 36, 252-260, 2009.

Fraser, A., Palmer, P. I., Feng, L., Boesch, H., Cogan, A., Parker, R., Dlugokencky, E. J., Fraser, P. J., Krummel, P. B., Langenfelds, R. L., O'Doherty, S., Prinn, R. G., Steele, L. P., van der Schoot, M., and Weiss, R. F.: Estimating regional methane surface fluxes: the relative importance of surface and GOSAT mole fraction measurements, Atmos. Chem. Phys., 13, 5697-5713, 10.5194/acp-13-5697-2013, 2013.

Fung, I., John, J., Lerner, J., Matthews, E., Prather, M., Steele, L. P., and Fraser, P. J.: Three-dimensional model synthesis of the global methane cycle, J. Geophys. Res.-Atmos., 96, 13033-13065, 1991.

He, J., Naik, V., Horowitz, L. W., Dlugokencky, E., and Thoning, K.: Investigation of the global methane budget over 1980–2017 using GFDL-AM4.1, Atmos. Chem. Phys., 20, 805-827, 10.5194/acp-20-805-2020, 2020.

Hoesly, R. M., Smith, S. J., Feng, L., Klimont, Z., Janssens-Maenhout, G., Pitkanen, T., Seibert, J. J., Vu, L., Andres, R. J., Bolt, R. M., Bond, T. C., Dawidowski, L., Kholod, N., Kurokawa, J.-i., Li, M., Liu, L., Lu, Z., Moura, M. C. P., O'Rourke, P. R., and Zhang, Q.: Historical (1750–2014) anthropogenic emissions of reactive gases and aerosols from the Community Emissions Data System (CEDS), Geosci. Model Dev., 11, 369-408, 10.5194/gmd-11-369-2018, 2018.

IPCC: Carbon and other biogeochemical cycles, in: Climate Change 2013: The Physical Science Basis. Contribution of Working Group I to the Fifth Assessment Report of the Intergovernmental Panel on Climate Change, edited by: Stocker, T. F., Qin, D., Plattner, G.-K., Tignor, M., Allen, S. K., Boschung, J., Nauels, A., Xia, Y., Bex, V., and Midgley, P. M., Cambridge University Press, Cambridge, United Kingdom and New York, NY, USA, 465-570, 10.1017/cbo9781107415324.022, 2013.

Jackson, R. B., Saunois, M., Bousquet, P., Canadell, J. G., Poulter, B., Stavert, A. R., Bergamaschi, P., Niwa, Y., Segers, A., and Tsuruta, A.: Increasing anthropogenic methane emissions arise equally from agricultural and fossil fuel sources, Environ. Res. Lett., 15, 10.1088/1748-9326/ab9ed2, 2020.

Janssens-Maenhout, G., Crippa, M., Guizzardi, D., Muntean, M., Schaaf, E., Dentener, F., Bergamaschi, P., Pagliari, V., Olivier, J. G. J., Peters, J. A. H. W., van Aardenne, J. A., Monni, S., Doering, U., Petrescu, A. M. R., Solazzo, E., and Oreggioni, G. D.: EDGAR v4.3.2 Global Atlas of the three major greenhouse gas emissions for the period 1970–2012, Earth Syst. Sci. Data, 11, 959-1002, 10.5194/essd-11-959-2019, 2019.

Kirschke, S., Bousquet, P., Ciais, P., Saunois, M., Canadell, J. G., Dlugokencky, E. J., Bergamaschi, P., Bergmann, D., Blake, D. R., Bruhwiler, L., Cameron-Smith, P., Castaldi, S., Chevallier, F., Feng, L., Fraser, A., Heimann, M., Hodson, E. L., Houweling, S., Josse, B., Fraser, P. J., Krummel, P. B., Lamarque, J.-F., Langenfelds, R. L., Le Quéré, C., Naik, V., O'Doherty, S., Palmer, P. I., Pison, I., Plummer, D., Poulter, B., Prinn, R. G., Rigby, M., Ringeval, B., Santini, M., Schmidt, M., Shindell, D. T., Simpson, I. J., Spahni, R., Steele, L. P., Strode, S. A., Sudo, K., Szopa, S., van der Werf, G. R., Voulgarakis, A., van Weele, M., Weiss, R. F., Williams, J. E., and Zeng, G.: Three decades of global methane sources and sinks, Nat. Geosci., 6, 813-823, 10.1038/ngeo1955, 2013.

Kuze, A., Suto, H., Shiomi, K., Kawakami, S., Tanaka, M., Ueda, Y., Deguchi, A., Yoshida, J., Yamamoto, Y., Kataoka, F., Taylor, T. E., and Buijs, H. L.: Update on GOSAT TANSO-FTS performance, operations, and data products after more than 6 years in space, Atmos. Meas. Tech., 9, 2445-2461, 10.5194/amt-9-2445-2016, 2016.

Liu, G., Peng, S., Lin, X., Ciais, P., Li, X., Xi, Y., Lu, Z., Chang, J., Saunois, M., Wu, Y., Patra, P., Chandra, N., Zeng, H., and Piao, S.: Recent Slowdown of Anthropogenic Methane Emissions in China Driven by Stabilized Coal Production, Environ. Sci. Technol. Lett., 8, 739-746, 10.1021/acs.estlett.1c00463, 2021.

Lu, X., Jacob, D. J., Zhang, Y., Maasakkers, J. D., Sulprizio, M. P., Shen, L., Qu, Z., Scarpelli, T. R., Nesser, H., Yantosca, R. M., Sheng, J., Andrews, A., Parker, R. J., Boesch, H., Bloom, A. A., and Ma, S.: Global methane budget and trend, 2010–2017: complementarity of inverse analyses using in situ (GLOBALVIEWplus CH_4 and satellite (GOSAT) observations, Atmos. Chem. Phys., 21, 4637-4657, 10.5194/acp-21-4637-2021, 2021.

Maasakkers, J. D., Jacob, D. J., Sulprizio, M. P., Scarpelli, T. R., Nesser, H., Sheng, J., Zhang, Y., Lu, X., Bloom, A. A., Bowman, K. W., Worden, J. R., and Parker, R. J.: 2010–2015 North American methane emissions, sectoral contributions, and

10   trends: a high-resolution inversion of GOSAT observations of atmospheric methane, Atmos. Chem. Phys., 21, 4339-4356, 10.5194/acp-21-4339-2021, 2021.

Maasakkers, J. D., Jacob, D. J., Sulprizio, M. P., Scarpelli, T. R., Nesser, H., Sheng, J.-X., Zhang, Y., Hersher, M., Bloom, A. A., Bowman, K. W., Worden, J. R., Janssens-Maenhout, G., and Parker, R. J.: Global distribution of methane emissions, emission trends, and OH concentrations and trends inferred from an inversion of GOSAT satellite data for 2010–2015, Atmos.

15   Chem. Phys., 19, 7859-7881, 10.5194/acp-19-7859-2019, 2019.

Maasakkers, J. D., Jacob, D. J., Sulprizio, M. P., Turner, A. J., Weitz, M., Wirth, T., Hight, C., DeFigueiredo, M., Desai, M., Schmeltz, R., Hockstad, L., Bloom, A. A., Bowman, K. W., Jeong, S., and Fischer, M. L.: Gridded National Inventory of U.S. Methane Emissions, Environ Sci Technol, 50, 13123-13133, 10.1021/acs.est.6b02878, 2016.

Miller, S. M., Michalak, A. M., Detmers, R. G., Hasekamp, O. P., Bruhwiler, L. M. P., and Schwietzke, S.: China's coal mine

20   methane regulations have not curbed growing emissions, Nat. Commun., 10, 303, 10.1038/s41467-018-07891-7, 2019.

Murray, L. T., Jacob, D. J., Logan, J. A., Hudman, R. C., and Koshak, W. J.: Optimized regional and interannual variability of lightning in a global chemical transport model constrained by LIS/OTD satellite data, J. Geophys. Res.-Atmos., 117, 10.1029/2012jd017934, 2012.

Nisbet, E. G., Manning, M. R., Dlugokencky, E. J., Fisher, R. E., Lowry, D., Michel, S. E., Myhre, C. L., Platt, S. M., Allen,

25   G., Bousquet, P., Brownlow, R., Cain, M., France, J. L., Hermansen, O., Hossaini, R., Jones, A. E., Levin, I., Manning, A. C., Myhre, G., Pyle, J. A., Vaughn, B. H., Warwick, N. J., and White, J. W. C.: Very Strong Atmospheric Methane Growth in the 4 Years 2014–2017: Implications for the Paris Agreement, Global Biogeochem. Cy., 33, 318-342, 10.1029/2018gb006009, 2019.

Nisbet, E. G., Dlugokencky, E. J., Manning, M. R., Lowry, D., Fisher, R. E., France, J. L., Michel, S. E., Miller, J. B., White,

30   J. W. C., Vaughn, B., Bousquet, P., Pyle, J. A., Warwick, N. J., Cain, M., Brownlow, R., Zazzeri, G., Lanoisellé, M., Manning, A. C., Gloor, E., Worthy, D. E. J., Brunke, E. G., Labuschagne, C., Wolff, E. W., and Ganesan, A. L.: Rising atmospheric methane: 2007-2014 growth and isotopic shift, Global Biogeochem. Cy., 30, 1356-1370, 10.1002/2016gb005406, 2016.

Pandey, S., Houweling, S., Krol, M., Aben, I., Chevallier, F., Dlugokencky, E. J., Gatti, L. V., Gloor, E., Miller, J. B., Detmers, R., Machida, T., and Röckmann, T.: Inverse modeling of GOSAT-retrieved ratios of total column CH_4 and CO_2 for 2009 and

35   2010, Atmos. Chem. Phys., 16, 5043-5062, 10.5194/acp-16-5043-2016, 2016.

Parker, R. J., Boesch, H., Byckling, K., Webb, A. J., Palmer, P. I., Feng, L., Bergamaschi, P., Chevallier, F., Notholt, J., Deutscher, N., Warneke, T., Hase, F., Sussmann, R., Kawakami, S., Kivi, R., Griffith, D. W. T., and Velazco, V.: Assessing 5 years of GOSAT Proxy XCH_4 data and associated uncertainties, Atmos. Meas. Tech., 8, 4785-4801, 10.5194/amt-8-4785-2015, 2015.

40   Parker, R. J., Webb, A., Boesch, H., Somkuti, P., Barrio Guillo, R., Di Noia, A., Kalaitzi, N., Anand, J. S., Bergamaschi, P., Chevallier, F., Palmer, P. I., Feng, L., Deutscher, N. M., Feist, D. G., Griffith, D. W. T., Hase, F., Kivi, R., Morino, I., Notholt, J., Oh, Y.-S., Ohyama, H., Petri, C., Pollard, D. F., Roehl, C., Sha, M. K., Shiomi, K., Strong, K., Sussmann, R., Té, Y.,

Velazco, V. A., Warneke, T., Wennberg, P. O., and Wunch, D.: A decade of GOSAT Proxy satellite CH_4 observations, Earth Syst. Sci. Data, 12, 3383-3412, 10.5194/essd-12-3383-2020, 2020.

45 Peng, S., Piao, S., Bousquet, P., Ciais, P., Li, B., Lin, X., Tao, S., Wang, Z., Zhang, Y., and Zhou, F.: Inventory of anthropogenic methane emissions in mainland China from 1980 to 2010, Atmos. Chem. Phys., 16, 14545-14562, 10.5194/acp-16-14545-2016, 2016.

Ridgwell, A. J., Marshall, S. J., and Gregson, K.: Consumption of atmospheric methane by soils: A process-based model, Global Biogeochem. Cy., 13, 59-70, Doi 10.1029/1998gb900004, 1999.

50 Saunois, M., Bousquet, P., Poulter, B., Peregon, A., Ciais, P., Canadell, J. G., Dlugokencky, E. J., Etiope, G., Bastviken, D., Houweling, S., Janssens-Maenhout, G., Tubiello, F. N., Castaldi, S., Jackson, R. B., Alexe, M., Arora, V. K., Beerling, D. J., Bergamaschi, P., Blake, D. R., Brailsford, G., Bruhwiler, L., Crevoisier, C., Crill, P., Covey, K., Frankenberg, C., Gedney, N., Höglund-Isaksson, L., Ishizawa, M., Ito, A., Joos, F., Kim, H.-S., Kleinen, T., Krummel, P., Lamarque, J.-F., Langenfelds, R., Locatelli, R., Machida, T., Maksyutov, S., Melton, J. R., Morino, I., Naik, V., O'Doherty, S., Parmentier, F.-J. W., Patra, P.

55 K., Peng, C., Peng, S., Peters, G. P., Pison, I., Prinn, R., Ramonet, M., Riley, W. J., Saito, M., Santini, M., Schroeder, R., Simpson, I. J., Spahni, R., Takizawa, A., Thornton, B. F., Tian, H., Tohjima, Y., Viovy, N., Voulgarakis, A., Weiss, R., Wilton, D. J., Wiltshire, A., Worthy, D., Wunch, D., Xu, X., Yoshida, Y., Zhang, B., Zhang, Z., and Zhu, Q.: Variability and quasi-decadal changes in the methane budget over the period 2000–2012, Atmos. Chem. Phys., 17, 11135-11161, 10.5194/acp-17-11135-2017, 2017.

60 Saunois, M., Bousquet, P., Poulter, B., Peregon, A., Ciais, P., Canadell, J. G., Dlugokencky, E. J., Etiope, G., Bastviken, D., Houweling, S., Janssens-Maenhout, G., Tubiello, F. N., Castaldi, S., Jackson, R. B., Alexe, M., Arora, V. K., Beerling, D. J., Bergamaschi, P., Blake, D. R., Brailsford, G., Brovkin, V., Bruhwiler, L., Crevoisier, C., Crill, P., Covey, K., Curry, C., Frankenberg, C., Gedney, N., Höglund-Isaksson, L., Ishizawa, M., Ito, A., Joos, F., Kim, H.-S., Kleinen, T., Krummel, P., Lamarque, J.-F., Langenfelds, R., Locatelli, R., Machida, T., Maksyutov, S., McDonald, K. C., Marshall, J., Melton, J. R.,

65 Morino, I., Naik, V., O'Doherty, S., Parmentier, F.-J. W., Patra, P. K., Peng, C., Peng, S., Peters, G. P., Pison, I., Prigent, C., Prinn, R., Ramonet, M., Riley, W. J., Saito, M., Santini, M., Schroeder, R., Simpson, I. J., Spahni, R., Steele, P., Takizawa, A., Thornton, B. F., Tian, H., Tohjima, Y., Viovy, N., Voulgarakis, A., van Weele, M., van der Werf, G. R., Weiss, R., Wiedinmyer, C., Wilton, D. J., Wiltshire, A., Worthy, D., Wunch, D., Xu, X., Yoshida, Y., Zhang, B., Zhang, Z., and Zhu, Q.: The global methane budget 2000–2012, Earth Syst. Sci. Data, 8, 697-751, 10.5194/essd-8-697-2016, 2016.

70 Saunois, M., Stavert, A. R., Poulter, B., Bousquet, P., Canadell, J. G., Jackson, R. B., Raymond, P. A., Dlugokencky, E. J., Houweling, S., Patra, P. K., Ciais, P., Arora, V. K., Bastviken, D., Bergamaschi, P., Blake, D. R., Brailsford, G., Bruhwiler, L., Carlson, K. M., Carrol, M., Castaldi, S., Chandra, N., Crevoisier, C., Crill, P. M., Covey, K., Curry, C. L., Etiope, G., Frankenberg, C., Gedney, N., Hegglin, M. I., Höglund-Isaksson, L., Hugelius, G., Ishizawa, M., Ito, A., Janssens-Maenhout, G., Jensen, K. M., Joos, F., Kleinen, T., Krummel, P. B., Langenfelds, R. L., Laruelle, G. G., Liu, L., Machida, T., Maksyutov,

75 S., McDonald, K. C., McNorton, J., Miller, P. A., Melton, J. R., Morino, I., Müller, J., Murguia-Flores, F., Naik, V., Niwa, Y., Noce, S., O'Doherty, S., Parker, R. J., Peng, C., Peng, S., Peters, G. P., Prigent, C., Prinn, R., Ramonet, M., Regnier, P., Riley,

W. J., Rosentreter, J. A., Segers, A., Simpson, I. J., Shi, H., Smith, S. J., Steele, L. P., Thornton, B. F., Tian, H., Tohjima, Y., Tubiello, F. N., Tsuruta, A., Viovy, N., Voulgarakis, A., Weber, T. S., van Weele, M., van der Werf, G. R., Weiss, R. F., Worthy, D., Wunch, D., Yin, Y., Yoshida, Y., Zhang, W., Zhang, Z., Zhao, Y., Zheng, B., Zhu, Q., Zhu, Q., and Zhuang, Q.: The Global Methane Budget 2000–2017, Earth Syst. Sci. Data, 12, 1561-1623, 10.5194/essd-12-1561-2020, 2020.

Sheng, J., Song, S., Zhang, Y., Prinn, R. G., and Janssens-Maenhout, G.: Bottom-Up Estimates of Coal Mine Methane Emissions in China: A Gridded Inventory, Emission Factors, and Trends, Environ. Sci. Technol. Lett., 10.1021/acs.estlett.9b00294, 2019.

Sheng, J., Tunnicliffe, R., Ganesan, A. L., Maasakkers, J. D., Shen, L., Prinn, R. G., Song, S., Zhang, Y., Scarpelli, T., Anthony Bloom, A., Rigby, M., Manning, A. J., Parker, R. J., Boesch, H., Lan, X., Zhang, B., Zhuang, M., and Lu, X.: Sustained methane emissions from China after 2012 despite declining coal production and rice-cultivated area, Environ. Res. Lett., 16, 10.1088/1748-9326/ac24d1, 2021.

Sherwen, T., Schmidt, J. A., Evans, M. J., Carpenter, L. J., Großmann, K., Eastham, S. D., Jacob, D. J., Dix, B., Koenig, T. K., Sinreich, R., Ortega, I., Volkamer, R., Saiz-Lopez, A., Prados-Roman, C., Mahajan, A. S., and Ordóñez, C.: Global impacts of tropospheric halogens (Cl, Br, I) on oxidants and composition in GEOS-Chem, Atmos. Chem. Phys., 16, 12239-12271, 10.5194/acp-16-12239-2016, 2016.

Stanevich, I., Jones, D. B. A., Strong, K., Parker, R. J., Boesch, H., Wunch, D., Notholt, J., Petri, C., Warneke, T., Sussmann, R., Schneider, M., Hase, F., Kivi, R., Deutscher, N. M., Velazco, V. A., Walker, K. A., and Deng, F.: Characterizing model errors in chemical transport modeling of methane: impact of model resolution in versions v9-02 of GEOS-Chem and v35j of its adjoint model, Geosci. Model Dev., 13, 3839-3862, 10.5194/gmd-13-3839-2020, 2020.

Thompson, R. L., Stohl, A., Zhou, L. X., Dlugokencky, E., Fukuyama, Y., Tohjima, Y., Kim, S. Y., Lee, H., Nisbet, E. G., Fisher, R. E., Lowry, D., Weiss, R. F., Prinn, R. G., O'Doherty, S., Young, D., and White, J. W. C.: Methane emissions in East Asia for 2000-2011 estimated using an atmospheric Bayesian inversion, J. Geophys. Res.-Atmos., 120, 4352-4369, 10.1002/2014jd022394, 2015.

Turner, A. J., Frankenberg, C., and Kort, E. A.: Interpreting contemporary trends in atmospheric methane, P. Natl. Acad. Sci. USA, 116, 2805-2813, 10.1073/pnas.1814297116, 2019.

Turner, A. J., Jacob, D. J., Benmergui, J., Wofsy, S. C., Maasakkers, J. D., Butz, A., Hasekamp, O., and Biraud, S. C.: A large increase in U.S. methane emissions over the past decade inferred from satellite data and surface observations, Geophys. Res. Lett., 43, 2218-2224, 10.1002/2016gl067987, 2016.

Turner, A. J., Jacob, D. J., Wecht, K. J., Maasakkers, J. D., Lundgren, E., Andrews, A. E., Biraud, S. C., Boesch, H., Bowman, K. W., Deutscher, N. M., Dubey, M. K., Griffith, D. W. T., Hase, F., Kuze, A., Notholt, J., Ohyama, H., Parker, R., Payne, V. H., Sussmann, R., Sweeney, C., Velazco, V. A., Warneke, T., Wennberg, P. O., and Wunch, D.: Estimating global and North American methane emissions with high spatial resolution using GOSAT satellite data, Atmos. Chem. Phys., 15, 7049-7069, 10.5194/acp-15-7049-2015, 2015.

Valentini, R., Arneth, A., Bombelli, A., Castaldi, S., Cazzolla Gatti, R., Chevallier, F., Ciais, P., Grieco, E., Hartmann, J., Henry, M., Houghton, R. A., Jung, M., Kutsch, W. L., Malhi, Y., Mayorga, E., Merbold, L., Murray-Tortarolo, G., Papale, D., Peylin, P., Poulter, B., Raymond, P. A., Santini, M., Sitch, S., Vaglio Laurin, G., van der Werf, G. R., Williams, C. A., and Scholes, R. J.: A full greenhouse gases budget of Africa: synthesis, uncertainties, and vulnerabilities, Biogeosciences, 11, 381-407, 10.5194/bg-11-381-2014, 2014.

Wecht, K. J., Jacob, D. J., Frankenberg, C., Jiang, Z., and Blake, D. R.: Mapping of North American methane emissions with high spatial resolution by inversion of SCIAMACHY satellite data, J. Geophys. Res.-Atmos., 119, 7741-7756, 10.1002/2014jd021551, 2014.

Wofsy, S. C., Team, T. H. S., Modellers, C., and Teams, S.: HIAPER Pole-to-Pole Observations (HIPPO): fine-grained, global-scale measurements of climatically important atmospheric gases and aerosols, Philosophical Transactions Mathematical Physical & Engineering Sciences, 369, 2073-2086, 2011.

Wofsy, S. C., Daube, B. C., Jimenez, R., Kort, E., Pittman, J. V., Park, S., Commane, R., Xiang, B., Santoni, G., Jacob, D., Fisher, J., Pickett-Heaps, C., Wang, H., Wecht, K., Wang, Q.-Q., Stephens, B. B., Shertz, S., Watt, A. S., Romashkin, P., Campos, T., HaGggerty, J., Cooper, W. A., Rogers, D., Beaton, S., Hendershot, R., Elkins, J. W., Fahey, D. W., Gao, R. S., Moore, F., Montzka, S. A., Schwarz, J. P., Perring, A. E., Hurst, D., Miller, B. R., Sweeney, C., Oltmans, S., Nance, D., Hintsa, E., Dutton, G., Watts, L. A., Spackman, J. R., Rosenlof, K. H., Ray, E. A., Hall, B., Zondlo, M. A., Diao, M., Keeling, R., Bent, J., Atlas, E. L., Lueb, R., and Mahoney, M. J.: HIPPO Merged 10-second Meteorology, Atmospheric Chemistry, Aerosol Data (R_20121129) [dataset], https://doi.org/10.3334/CDIAC/hippo_010, 2017.

Wofsy, S. C., Afshar, S., Allen, H. M., Apel, E. C., Asher, E. C., Barletta, B., Bent, J., Bian, H., Biggs, B. C., Blake, D. R., Blake, N., Bourgeois, I., Brock, C. A., Brune, W. H., Budney, J. W., Bui, T. P., Butler, A., Campuzano-Jost, P., Chang, C. S., Chin, M., Commane, R., Correa, G., Crounse, J. D., Cullis, P. D., Daube, B. C., Day, D. A., Dean-Day, J. M., Dibb, J. E., DiGangi, J. P., Diskin, G. S., Dollner, M., Elkins, J. W., Erdesz, F., Fiore, A. M., Flynn, C. M., Froyd, K. D., Gesler, D. W., Hall, S. R., Hanisco, T. F., Hannun, R. A., Hills, A. J., Hintsa, E. J., Hoffman, A., Hornbrook, R. S., Huey, L. G., Hughes, S., Jimenez, J. L., Johnson, B. J., Katich, J. M., Keeling, R. F., Kim, M. J., Kupc, A., Lait, L. R., Lamarque, J. F., Liu, J., McKain, K., McLaughlin, R. J., Meinardi, S., Miller, D. O., Montzka, S. A., Moore, F. L., Morgan, E. J., Murphy, D. M., Murray, L. T., Nault, B. A., Neuman, J. A., Newman, P. A., Nicely, J. M., Pan, X., Paplawsky, W., Peischl, J., Prather, M. J., Price, D. J., Ray, E. A., Reeves, J. M., Richardson, M., Rollins, A. W., Rosenlof, K. H., Ryerson, T. B., Scheuer, E., Schill, G. P., Schroder, J. C., Schwarz, J. P., St.Clair, J. M., Steenrod, S. D., Stephens, B. B., Strode, S. A., Sweeney, C., Tanner, D., Teng, A. P., Thames, A. B., Thompson, C. R., Ullmann, K., Veres, P. R., Vieznor, N., Wagner, N. L., Watt, A., Weber, R., Weinzierl, B., Wennberg, P. O., Williamson, C. J., Wilson, J. C., Wolfe, G. M., Woods, C. T., and Zeng, L. H.: ATom: Merged Atmospheric Chemistry, Trace Gases, and Aerosols, 10.3334/ORNLDAAC/1581, 2018.

Worden, J. R., Bloom, A. A., Pandey, S., Jiang, Z., Worden, H. M., Walker, T. W., Houweling, S., and Rockmann, T.: Reduced biomass burning emissions reconcile conflicting estimates of the post-2006 atmospheric methane budget, Nat. Commun., 8, 2227, 10.1038/s41467-017-02246-0, 2017.

Wunch, D., Toon, G. C., Blavier, J. F., Washenfelder, R. A., Notholt, J., Connor, B. J., Griffith, D. W., Sherlock, V., and Wennberg, P. O.: The total carbon column observing network, Philos Trans A Math Phys Eng Sci, 369, 2087-2112, 10.1098/rsta.2010.0240, 2011.

Xu, X. and Tian, H.: Methane exchange between marshland and the atmosphere over China during 1949-2008, Global Biogeochem. Cy., 26, n/a-n/a, 10.1029/2010gb003946, 2012.

Yin, Y., Chevallier, F., Ciais, P., Bousquet, P., Saunois, M., Zheng, B., Worden, J., Bloom, A. A., Parker, R. J., Jacob, D. J., Dlugokencky, E. J., and Frankenberg, C.: Accelerating methane growth rate from 2010 to 2017: leading contributions from the tropics and East Asia, Atmos. Chem. Phys., 21, 12631-12647, 10.5194/acp-21-12631-2021, 2021.

Yu, X., Millet, D. B., Wells, K. C., Henze, D. K., Cao, H., Griffis, T. J., Kort, E. A., Plant, G., Deventer, M. J., Kolka, R. K., Roman, D. T., Davis, K. J., Desai, A. R., Baier, B. C., McKain, K., Czarnetzki, A. C., and Bloom, A. A.: Aircraft-based inversions quantify the importance of wetlands and livestock for Upper Midwest methane emissions, Atmos Chem Phys, 21, 951-971, 10.5194/acp-21-951-2021, 2021.

Zhang, B., Tian, H., Ren, W., Tao, B., Lu, C., Yang, J., Banger, K., and Pan, S.: Methane emissions from global rice fields: Magnitude, spatiotemporal patterns, and environmental controls, Global Biogeochem. Cy., 30, 1246-1263, 10.1002/2016gb005381, 2016.

Zhang, Y., Jacob, D. J., Lu, X., Maasakkers, J. D., Scarpelli, T. R., Sheng, J.-X., Shen, L., Qu, Z., Sulprizio, M. P., Chang, J., Bloom, A. A., Ma, S., Worden, J., Parker, R. J., and Boesch, H.: Attribution of the accelerating increase in atmospheric methane during 2010–2018 by inverse analysis of GOSAT observations, Atmos. Chem. Phys., 21, 3643-3666, 10.5194/acp-21-3643-2021, 2021.

Zhao, Y., Saunois, M., Bousquet, P., Lin, X., Hegglin, M. I., Canadell, J. G., Jackson, R. B., Hauglustaine, D. A., Szopa, S., Stavert, A. R., Abraham, N. L., Archibald, A. T., Bekki, S., Deushi, M., Jöckel, P., Josse, B., Kinnison, D., Kirner, O., Marécal, V., amp, apos, Connor, F. M., Plummer, D. A., Revell, L. E., Rozanov, E., Stenke, A., Strode, S., Tilmes, S., Dlugokencky, E. J., and Zheng, B.: Inter-model comparison of global hydroxyl radical (OH) distributions and their impact on atmospheric methane over the 2000-2016 period, Atmos. Chem. Phys. Discuss., 1-47, 10.5194/acp-2019-281, 2019.

Tables and Figures

Table 1. CH$_4$ measurements and GEOS-Chem model simulations at four NOAA surface sites over China.

Case	Resolution	Emission	OH	DSI (20.7ºN, 116.7ºE) 2010.03–2018.12		LLN (23.5ºN, 120.9ºE) 2006.08–2018.12		SDZ (40.7ºN, 117.1ºE) 2009.09–2015.09		WLG (36.3ºN, 100.9ºE) 2000.01–2006.12	2007.01–2018.12	
				Mean	Trend	Mean	Trend	Mean	Trend	Mean	Mean	Trend
Obs.	/	/	/	1884.8	7.94	1851.7	7.03	1954.6	7.13	1832.4	1878.4	7.25
Run1	4º×5º	EDGAR	Fixed	+0.4%	8.74 (+0.8)	−3.3%	9.63 (+2.6)	−2.9%	13.33 (+6.2)	−5.5%	−3.6%	9.35 (+2.1)
Run2	4º×5º	CEDS	Fixed	+4.4%	11.94 (+4.0)	+0.4%	13.23 (+6.2)	+2.3%	18.03 (+10.9)	−3.8%	+0.2%	12.85 (+5.6)
Run3	4º×5º	EDGAR	Varying	+0.7%	4.24 (−3.7)	−2.5%	4.83 (−2.2)	−2.1%	8.23 (+1.1)	−2.6%	−2.9%	4.55 (−2.7)
Run4	4º×5º	CEDS	Varying	+4.6%	7.34 (−0.6)	+1.2%	8.33 (+1.3)	+3.0%	12.73 (+5.6)	−1.0%	+0.9%	7.95 (+0.7)
Run5	4º×5º	CEDS	Varying (−10% over 2010–2018)	+8.0%	19.14 (+11.2)	+3.5%	18.53 (+11.5)	+5.0%	25.93 (+18.8)	−1.0%	+3.4%	18.85 (+11.6)
Run6	4º×5º	CEDS	Varying (+10% over 2010–2018)	+1.4%	−3.56 (−11.5)	−1.1%	−1.17 (−8.2)	+1.1%	0.23 (−6.9)	−1.0%	−1.5%	−2.25 (−9.5)
Run7	4º×5º	CEDS (−50 Tg over 2010–2018)	Varying	+0.8%	−4.16 (−12.1)	−1.3%	−1.87 (−8.9)	+0.3%	−2.27 (−9.4)	−1.0%	−1.8%	−3.15 (−10.4)
GCE	2º×2.5º	EDGAR	Varying	−2.0%	3.54 (−4.4)	−1.5%	4.63 (−2.4)	+1.8%	9.73 (+2.6)	−2.6%	−2.8%	4.65 (−2.6)
GCC	2º×2.5º	CEDS	Varying	+1.6%	6.44 (−1.5)	+1.6%	8.13 (+1.1)	+6.5%	14.73 (+7.6)	−1.6%	+0.3%	7.95 (+0.7)

675   **Table 2. CH$_4$ sources and sinks over China in 2000s and 2010s[a].**

		Saunois et al. (2020)				Peng et al. (2016)	This study			
Time period		2000–2009		2008–2017		2000–2009	2000–2009		2008–2017	
Approach		B-U	T-D	B-U	T-D	B-U	GCE	GCC	GCE	GCC
Sources (Tg a^{-1})	Agriculture and waste	27.1 (24.0–33.0)	23.2 (10.4–28.3)	29.7 (25.8–37.2)	27.7 (10.9–34.7)	22.9	33.3	25.3	36.8	28.2
	Biomass and biofuel burning	3.3 (1.8–5.0)	3.6 (0.3–4.9)	3.2 (1.3–5.1)	3.7 (0.3–5.0)	2.3	4.8	3.6	4.8	3.9
	Fossil fuels	17.9 (12.6–23.9)	13.3 (7.4–31.0)	26.1 (16.6–39.6)	19.0 (8.0–35.6)	12.8	15.8	23.4	22.8	38.4
	Wetlands	2.6 (0.9–9.3)	6.0 (2.7–12.5)	2.6 (0.8–9.2)	5.2 (2.0–13.1)	/	2.8		2.8	
	Other sources	/	0.8 (0.6–1.6)	/	0.8 (0.5–1.6)	/	0.5	0.4	0.4	0.4
Sinks (Tg a^{-1})	Soils	/	1.5 (0.8–2.0)	/	1.8 (0.8–2.2)	/	0.9		0.9	
	OH chemical loss	/	8	/	/	/	6.3	6.4	6.7	6.9

[a] Bottom-up (B-U) and top-down (T-D) sources and soil uptake estimates of mean (range) values reported from Saunois et al., (2020) and Peng et al., (2016). OH chemical loss estimates in 2000s are from Kirschke et al., (2013).

680

685

Table 3. Sources contributing to the mean surface CH$_4$ mixing ratio in China over 2007–2018[a]

Concentration [%]	AGR	ENE	WST	RCO	BBN	WTL	SEE	TER	OTH	TOT
China	3.4	6.4	2.3	0.8	0.1	0.6	0.1	0.2	0.1	14.0
India	3.7	0.5	1.0	0.3	0.0	0.5	0.0	0.1	0.0	6.2
Rest Asia	3.7	1.6	1.6	0.3	0.3	5.0	0.1	0.2	0.0	12.8
Europe	3.2	5.8	2.4	0.2	0.2	2.7	0.2	0.2	0.1	15.0
Africa	2.7	4.9	1.3	0.4	1.3	5.5	0.2	0.7	0.0	17.0
North America	2.1	2.7	1.5	0.1	0.1	6.1	0.2	0.2	0.0	13.0
South America	4.1	3.4	1.1	0.1	0.4	10.5	0.2	0.5	0.0	20.2
Oceania	0.7	0.2	0.1	0.0	0.2	0.3	0.0	0.1	0.0	1.7
Rest World	0.0	0.0	0.0	0.0	0.0	0.0	0.0	0.0	0.0	0.1
Total	23.5	25.7	11.3	2.3	2.5	31.3	0.9	2.2	0.3	100

690   [a] Percentage contributions of CH$_4$ emissions from the CEDS sectors (Table S2) including agriculture (AGR), energy (ENE), wastewater (WST), residents (RCO), biomass burning (BBN), wetlands (WTL), seeps (SEE), termites (TER), and others (OTH) including industry (IND), transportation (TRA) and shipping (SHP), and from different regions (Fig. 2). Values are estimated using the tagged CH$_4$ tracer simulation.

695

700

705

710

Table 4. Contributions of region- and sector-specific emissions to the surface CH$_4$ trends in China over 2007–2018[a]

Trend [ppbv a^{-1}]	AGR	ENE	WST	RCO	WTL	OTH	Total
China	0.30	5.54	0.68	−0.04	0.01	0.01	6.50
India	0.56	0.32	0.32	0.05	−0.03	0.00	1.21
Rest Asia	0.62	0.92	0.44	0.00	−0.07	0.03	1.93
Europe	−0.81	−0.49	−0.40	−0.07	−0.08	0.05	−1.81
Africa	0.91	0.93	0.49	0.12	−0.75	−0.05	1.64
North America	−0.09	−0.10	−0.16	−0.01	−0.32	0.06	−0.63
South America	0.57	0.50	0.20	0.00	−0.35	0.04	0.95
Oceania	−0.07	0.05	−0.03	−0.01	0.00	−0.01	−0.07
Rest World	0.00	0.01	0.00	0.00	0.00	0.00	0.02
Total	1.98	7.68	1.54	0.03	−1.61	0.12	9.75

[a] Contributions of CH$_4$ sources from different CEDS sectors and from different regions to the mean surface trends in China over 2007–2018. The CEDS sectors include agriculture (AGR), energy (ENE), wastewater (WST), residents (RCO), wetland (WTL), and others (OTH) combining industry, transportation, shipping, biomass burning, seeps, and termites (Table S2). Values are estimated using the tagged CH$_4$ tracer simulation as described in the text.
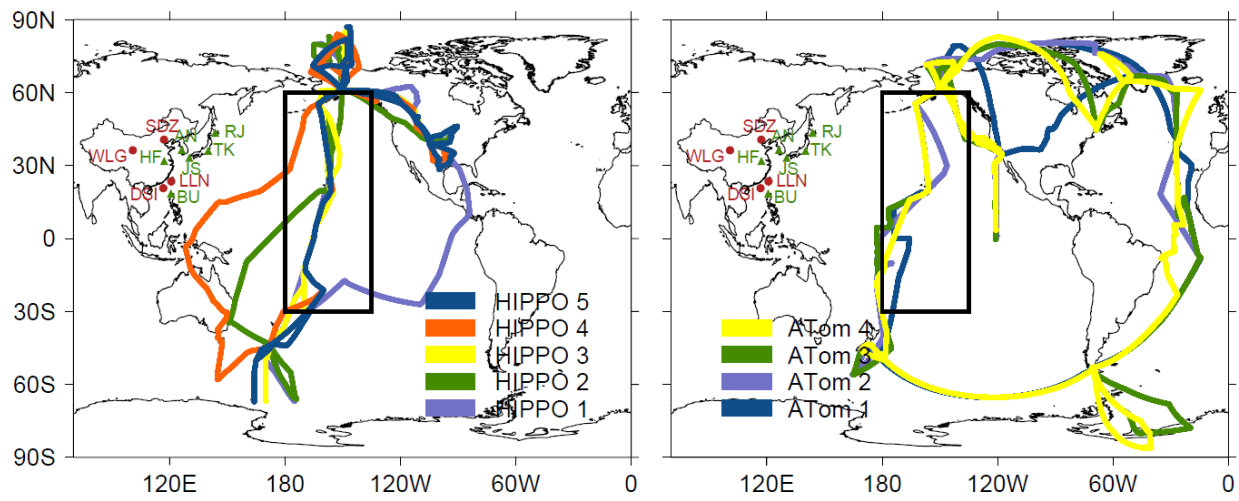
Figure 1. Locations of NOAA surface sites (red circles), TCCON sites (green triangles) in China and aircraft flight tracks of HIPPO and ATom campaigns.
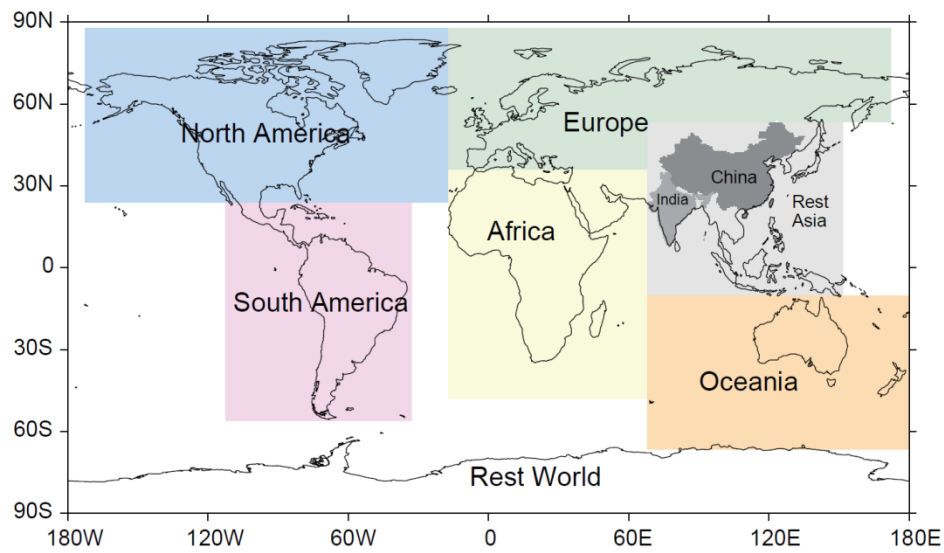
725 **Figure 2.** Regions defined in the tagged CH$_4$ tracer simulation. The regions are North America (NA), South America (SA), Europe (EU), Africa (AF), Oceania (OC), China (CHN), India (IND) and Rest Asia (RtAS). All other areas are included in the rest of the world (RW) region.
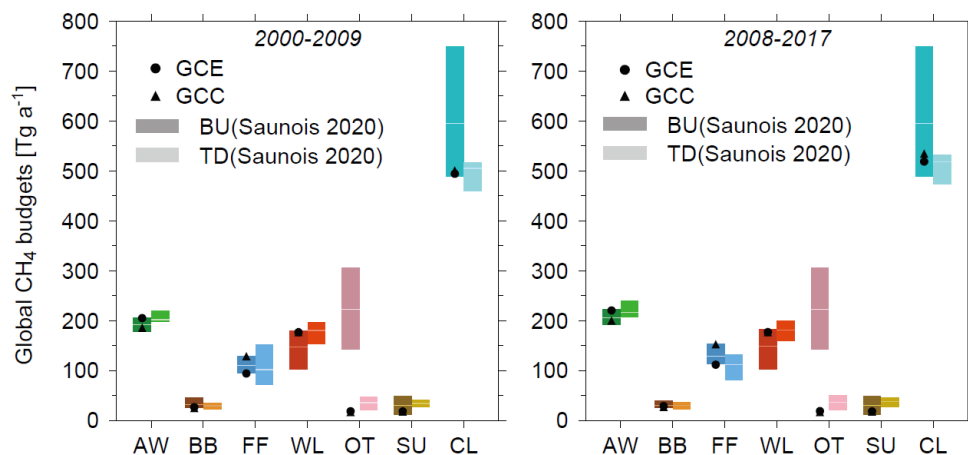
730 **Figure 3.** Global CH$_4$ budgets from main source categories and sinks for the 2000–2009 (2000s) and 2008–2017 (2010s) periods. Categories are grouped based on Table S2 including emissions from agriculture and waste (AW), fossil fuels (FF), wetlands (WL), biomass burning (BB), and others (OT), and sinks due to soil uptake (SU) and chemical loss (CL). The bar charts show bottom-up (dark-colored bars) and top-down (light-colored bars) estimates in previous studies as summarized by Saunois et al. (2020). The global CH$_4$ sources and sinks in the GCE (black circles) and GCC (black triangles) model simulations are also shown. Table S1 summarizes the values presented in the figure.

735
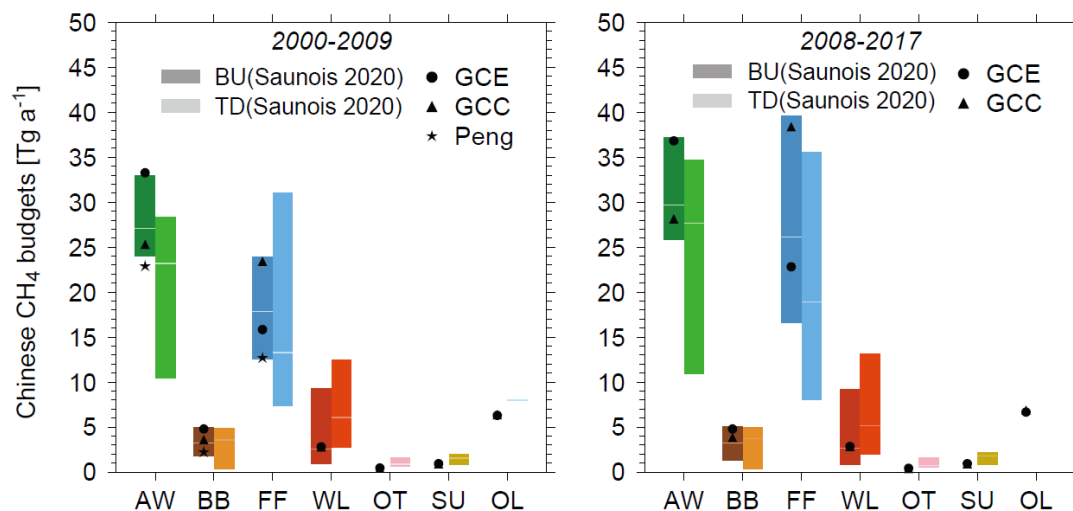
Figure 4. Similar to Fig. 3, but for CH$_4$ sources and sinks over China averaged for the 2000–2009 and 2008–2017 periods. The bar charts show previous Chinese bottom-up (dark-colored bars on the left) and top-down (light-colored bars on the right) estimates as summarized by Saunois et al. (2020) and Kirschke et al. (2013), and are compared with model results in the GCE (black circles) and GCC (black triangles) simulations. The bottom-up estimates of 2000–2009 mean Chinese CH$_4$ emissions by Peng et al. (2016) are also shown as black stars. Values presented in the figure are summarized in Table 2.

740
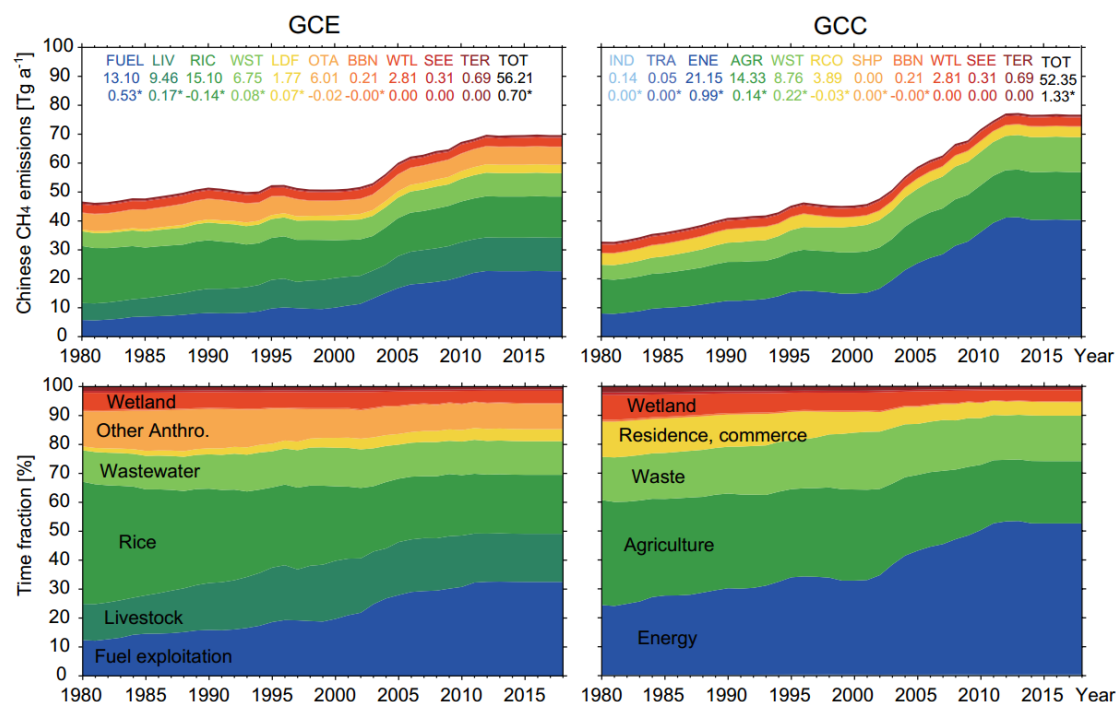
Figure 5. Time series of annual Chinese CH$_4$ emissions from different sectors (top panels) and their percentage contributions (bottom panels) in the GCE (left panels) and GCC (right panels) model simulations during the period of 1980–2018. The emission sectors and their abbreviations are listed in Table S2. Annual mean emission totals and trends over 1980–2018 (with asterisks denoting the statistical significance of p-value < 0.05) are shown inset.
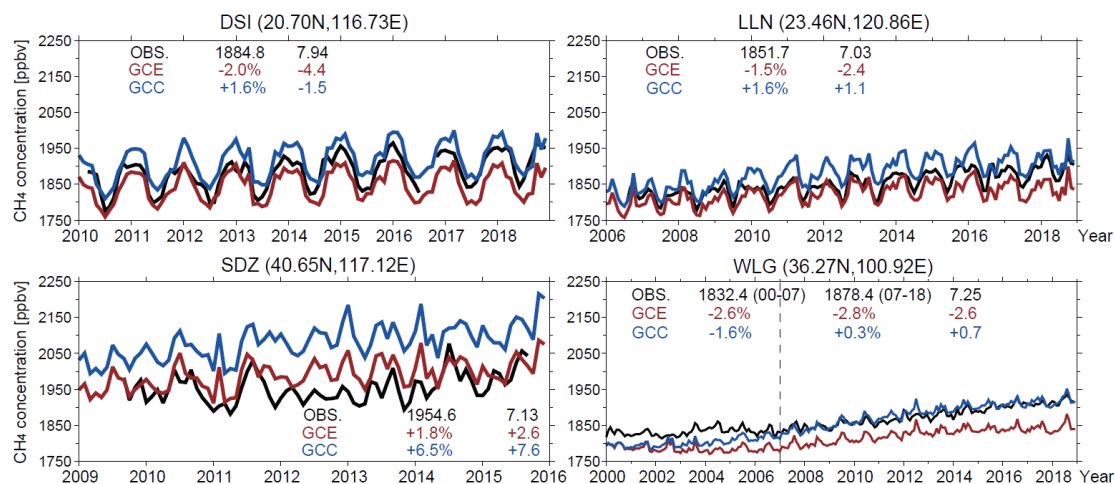
750   **Figure 6.** Comparison of GCE (with EDGAR anthropogenic emissions and interannually varying OH; red lines) and GCC (with CEDS and interannually varying OH; blue lines) simulated monthly mean CH_4 mixing ratios with NOAA in situ observations (black lines) in China. The observed mean mixing ratios (in unit of ppbv), trends (ppbv a^{-1}), and corresponding model biases are shown inset.
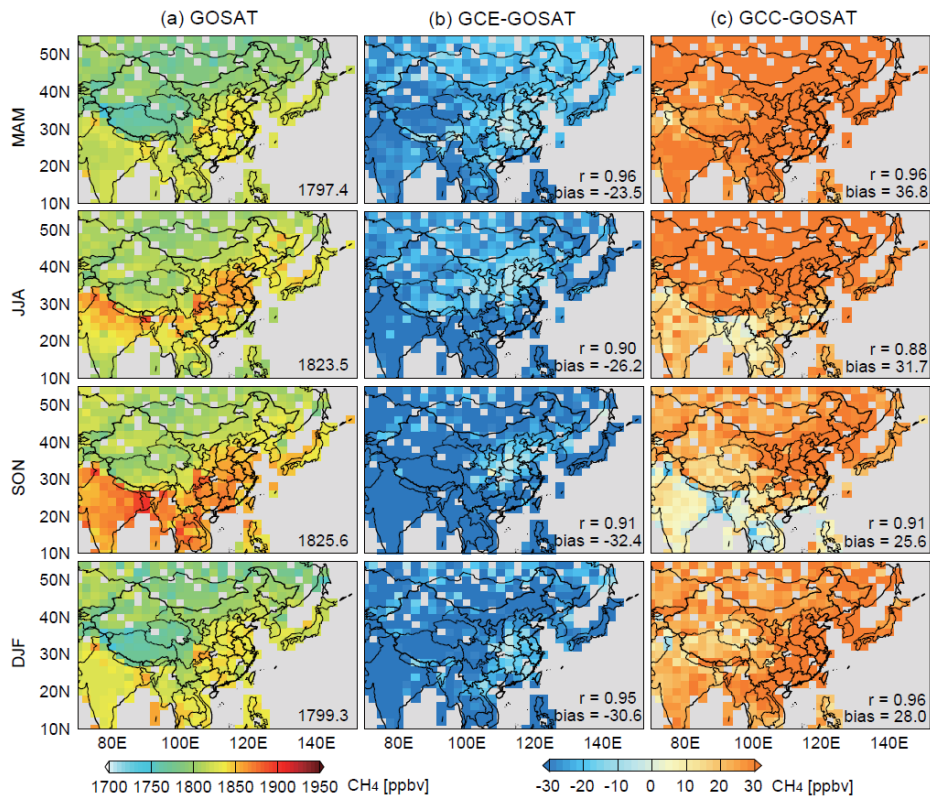
Figure 7. 2010–2017 seasonal mean GOSAT observed and model simulated atmospheric CH$_4$ mixing ratios over Asia. Both observations and the GEOS-Chem model simulations are regrided to the 2°×2.5° model resolution. The model results are then applied with satellite averaging kernels. The middle and right panels show, respectively, GCE (with EDGAR anthropogenic emissions and interannually varying OH; column b) minus GOSAT (column a) and GCC (with CEDS and interannually varying OH; column c) minus GOSAT differences. The observed mean atmospheric CH$_4$ mixing ratio, GOSAT vs. model correlation coefficients (*r*), and mean model biases over China are shown inset. The seasonal means are averages of March-April-May (MAM), June-July-August (JJA), September-October-November (SON), and December-January-February (DJF).
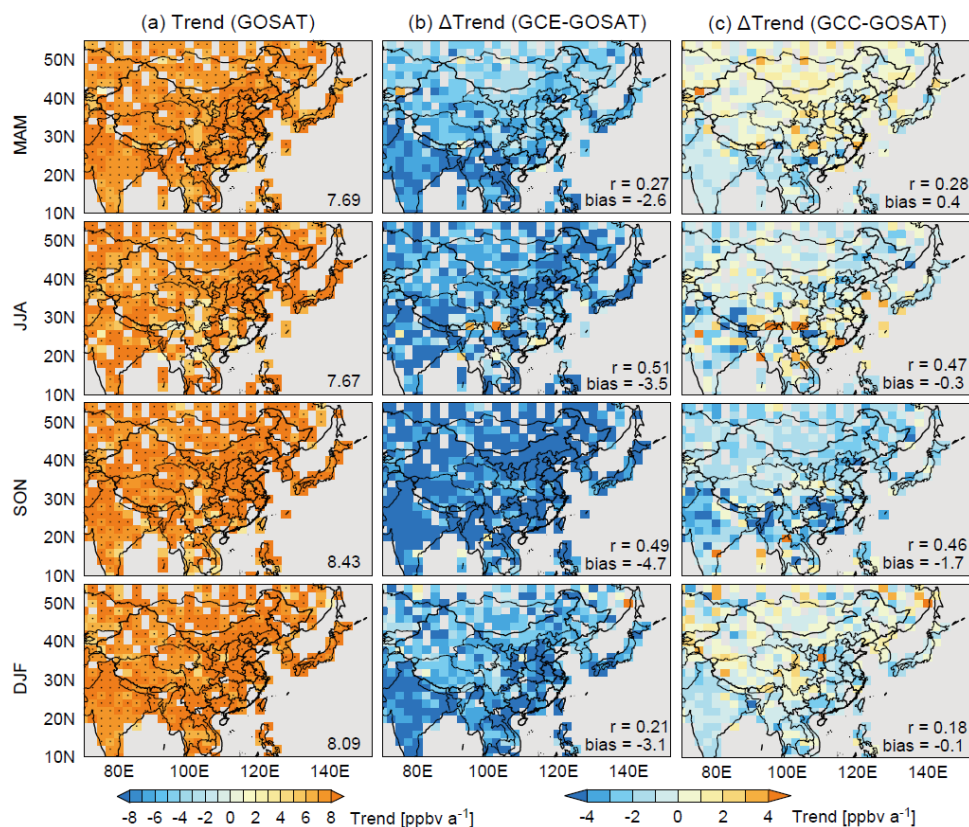
Figure 8. The same as Fig. 7, but for seasonal mean trends in atmospheric CH$_4$ mixing ratios over 2010–2017. The middle and right panels show, respectively, GCE (with EDGAR anthropogenic emissions and interannually varying OH; column b) minus GOSAT (column a) and GCC (with CEDS and interannually varying OH; column c) minus GOSAT differences. The observed mean CH$_4$ concentration trend, GOSAT vs. model correlation coefficients (r), and mean model biases over China are shown inset.
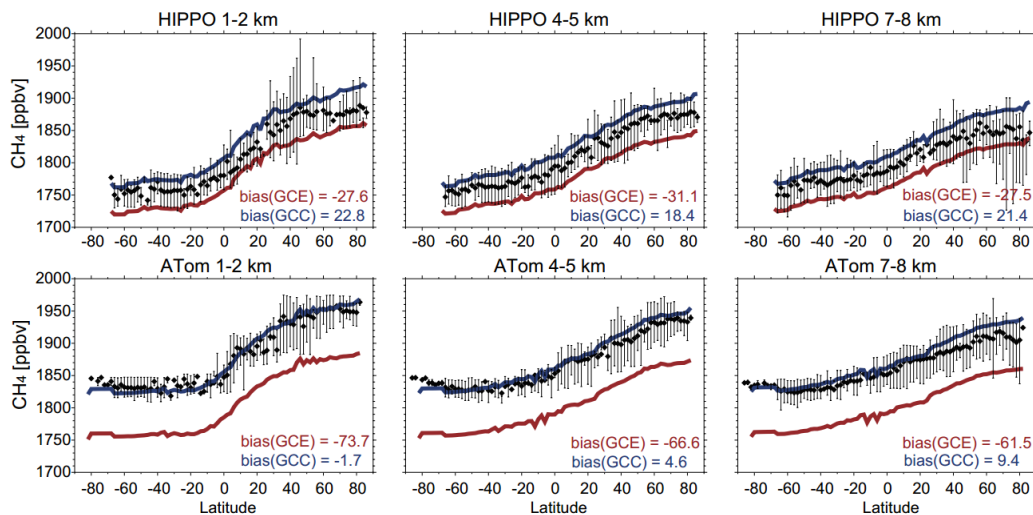
770 **Figure 9.** HIPPO and ATom aircraft measured latitudinal gradients of CH_4 mixing ratios. Measurements from HIPPO (top panels) and ATom (bottom panels) flights are averaged in 2° latitude bins and at three altitude levels (left: 1–2 km; middle: 4–5 km; and right: 7–8 km). The black symbols and bars represent the mean values and ranges for each bin. The corresponding model results from the GCE (with EDGAR anthropogenic emissions and interannually varying OH; red lines) and GCC (with CEDS and interannually varying OH; blue lines) simulations are also shown, and the values inset present the mean model biases relative to aircraft measurements.

775
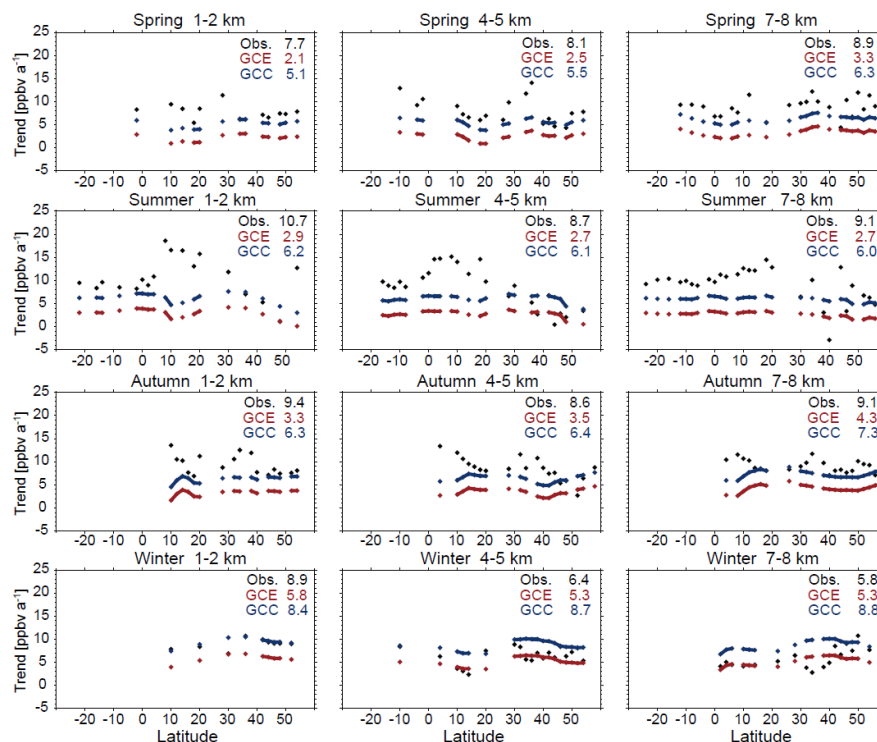
Figure 10. Comparisons of simulated CH$_4$ trends in GCE (with EDGAR anthropogenic emissions and interannually varying OH; red dots) and GCC (with CEDS and interannually varying OH; blue dots) against aircraft observation trends (black symbols) in four seasons (spring: March-April-May; summer: August; autumn: October-November; winter: January-February). All observations and model results sampled along the flight tracks are averaged in 2º latitude bins and at three altitude levels (left: 1–2 km; middle: 4–5 km; and right: 7–8 km). Mean observed and simulated CH$_4$ trends are shown inset.
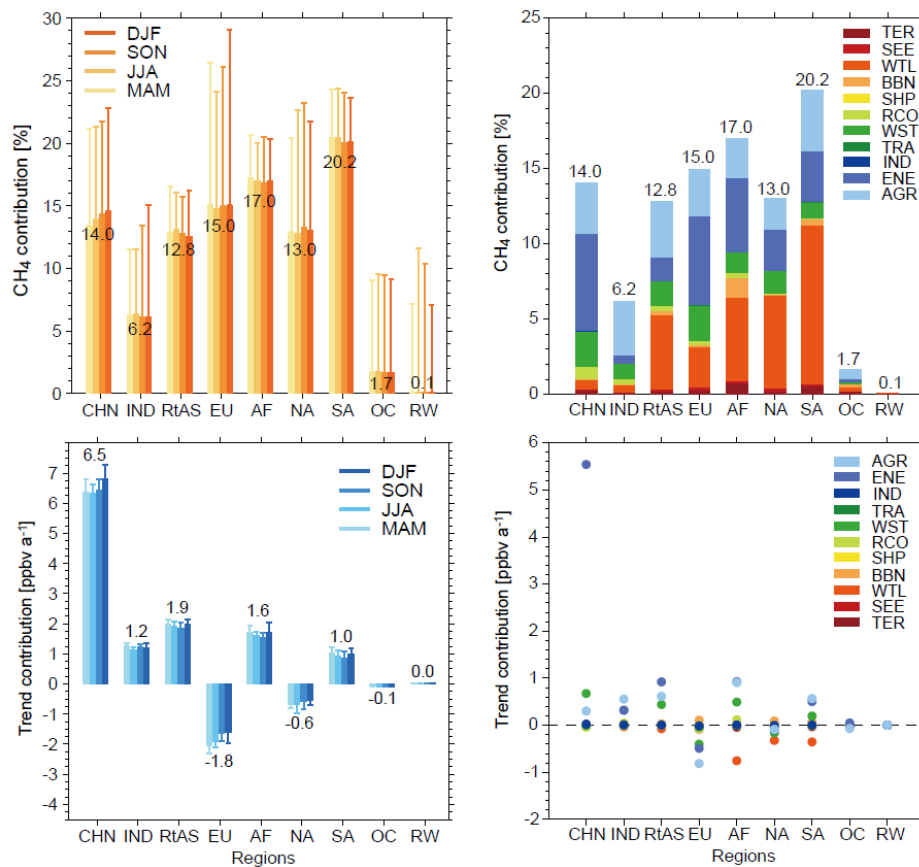
Figure 11. Contributions of CH₄ emissions from different regions and different source sectors on the mean surface CH₄ mixing ratios (top panels) and trends (bottom panels) in China over 2007–2018. The left panels show region-specific source contributions for different seasons and error bars are standard deviations denoting spatial variation of contributions over China. The right panels show region- and sector-specific contributions for the annual values. Source contributions are estimated using the tagged CH₄ tracers accounting for emission sources from agriculture (AGR), energy (ENE), industry (IND), transportation (TRA), residents (RCO), wastewater (WST), shipping (SHP), biomass burning (BBN), wetlands (WTL), seeps (SEE) and termites (TER) sectors and from nine regions (Africa, China, Europe, India, Asia excluding China and India, Oceania, South America, North America and the rest of the world).
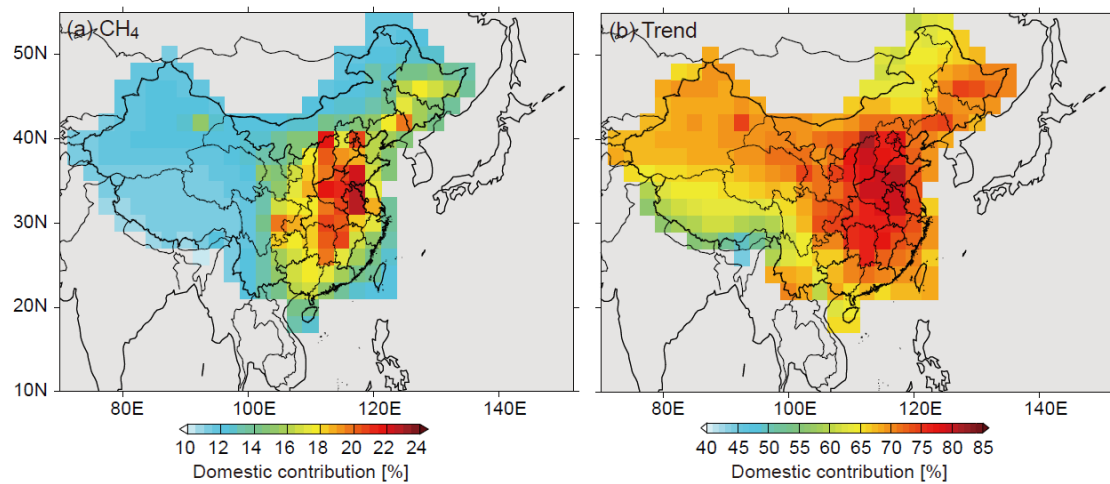
Figure 12. Spatial distributions of Chinese domestic emission contributions in percentage on CH$_4$ surface mixing ratios (a) and trends (b) in 2007–2018 over China. The percentage contributions are estimated by summing up all the Chinese tagged CH$_4$ tracers divided by the total CH$_4$ tracers in the tagged simulation.

795